Journal of Manufacturing Processes 70 (2021) 271–289

Contents lists available at ScienceDirect

Journal of Manufacturing Processes

journal homepage: www.elsevier.com/locate/manpro

A combined theoretical and experimental approach to model polyamide 12 degradation in selective laser sintering additive manufacturing

Feifei Yang, Xu Chen *

Department of Mechanical Engineering, University of Washington, Seattle, WA 98195, USA

ARTICLE INFO

Keywords:
Kinetic modelling
Polyamide 12
Thermal oxidation
Coupled oxygen and laser effects
Selective laser sintering

ABSTRACT

Selective laser sintering (SLS) generates complex high-performance parts from micrometer-diameter powders. In polyamide 12 SLS, a considerable amount of expensive polyamide 12 materials remains un-joined in the additive manufacturing (AM) process. Such materials, particularly the ones near the heat-affected zones (HAZ), go through irreversible chemical degradations originated from thermal oxidations. Despite efforts in understanding the degradation mechanisms of the materials, full modelling of the complex material degradation remains not well understood. In this work, through a combined theoretical and experimental approach, we propose a first-instance kinetic model considering the effects of both oxygen and laser to model the material degradation in polyamide 12 SLS. By mapping the actual material degradation rates into the oxidation physics and data-driven parameter identification, we obtain the coefficients of the actual coupled oxygen and laser effects. Through sensitivity analysis, we derive the fitting equations between the sample degradation rates and the oxidation time. The proposed kinetic model can predict the oxidation rates of pure or mixed materials using two easily available parameters: materials density and oxidation time. We show that the laser effects are 4-time stronger than oxygen effects on polyamide 12 degradation. The predicted oxidation matches on average 89.53% with the actual SLS degradation rates, in contrast to a 34.48% accuracy from a basic autoxidation model. Besides, the paper identifies how coupling of oxygen, laser irradiation, and preheating impacts the rate of material degradation.

1. Introduction

Additive manufacturing (AM) is a collective term with unrivalled design freedom to fabricate functional applications by joining layers of materials on top of each other [1–3]. Selective laser sintering (SLS) is a popular powder-based AM process with superior potentials to produce products with high mechanical properties and good thermal stability compared to other 3D additive techniques [4,5]. The capability to process almost any material, including polymers, metals, ceramics, and many types of composites, further extends the popularity of SLS [6]. Supporting materials are not needed in SLS as the powders can directly act as support to the printed parts [7]. Resulting from the high flowability, high melting enthalpy, and sharp melting peak, polyamide 12 appears to be the most suitable material among the wide-ranging material scope applicable for SLS [8–10]. Polyamide 12 (and its compounds) takes up approximately 90% of complete industrial consumption [11].

The extensive usage of polyamide 12 powders in SLS results in a large amount of un-sintered powders after going through complex degradations [12–14]. Previous research revealed that irreversible oxidation and post-condensation dominate the aging process and change the polymer chemical structures by chain scission, branching, and chain cross-linking [13,15,16]. The macro-structural chain cross-linking attributes to an increase in the material molecular weight and a decrease in the melt flow index (MFI) [17,18]. As the molecular weight increases with the powder aging, melt viscosity also increases and powder flowability decreases [14,16]. Aging affects little the distribution of powder sizes but leads to the deteriorated thermal property and reduced surface morphology [13].

Despite the property changes, a considerable amount of un-sintered polyamide 12 residues (80% - 90%) has the potential to be reused for further applications [14]. One of the solutions to the successful reuse of SLS residue is to fabricate the powder residue into feedstock for other AM processes without significantly reducing its value. Polyamide 12 powder for SLS is priced at around $150/kg (in 2020 currency). The cost of extrusion-based additive manufacturing (EAM) or fused deposition modelling (FDM) polyamide 12 filament is approximate $100/kg, while the cost of polyamide 12 pellets for conventional plastics processing is

* Corresponding author.
E-mail address: chx@uw.edu (X. Chen).

https://doi.org/10.1016/j.jmapro.2021.08.051
Received 26 June 2021; Received in revised form 24 August 2021; Accepted 26 August 2021
Available online 3 September 2021

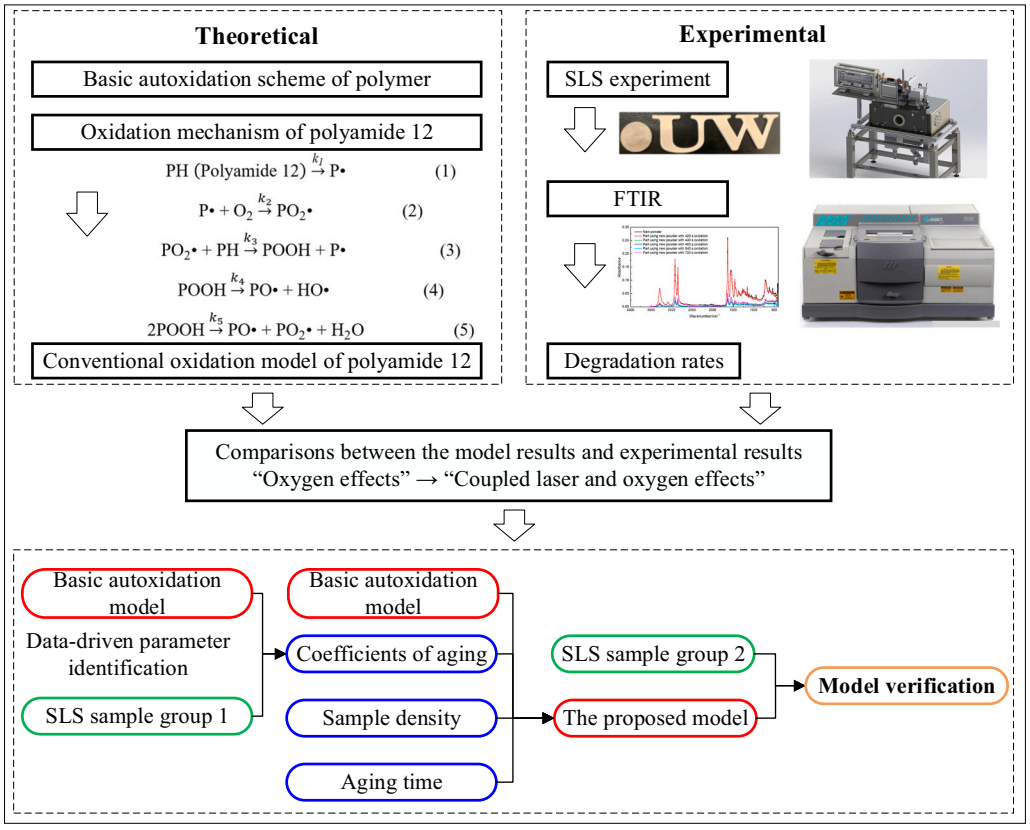

Fig. 1. The proposed approach to build the kinetic scheme of polyamide 12 aging in SLS considering the coupled oxygen and laser effects.

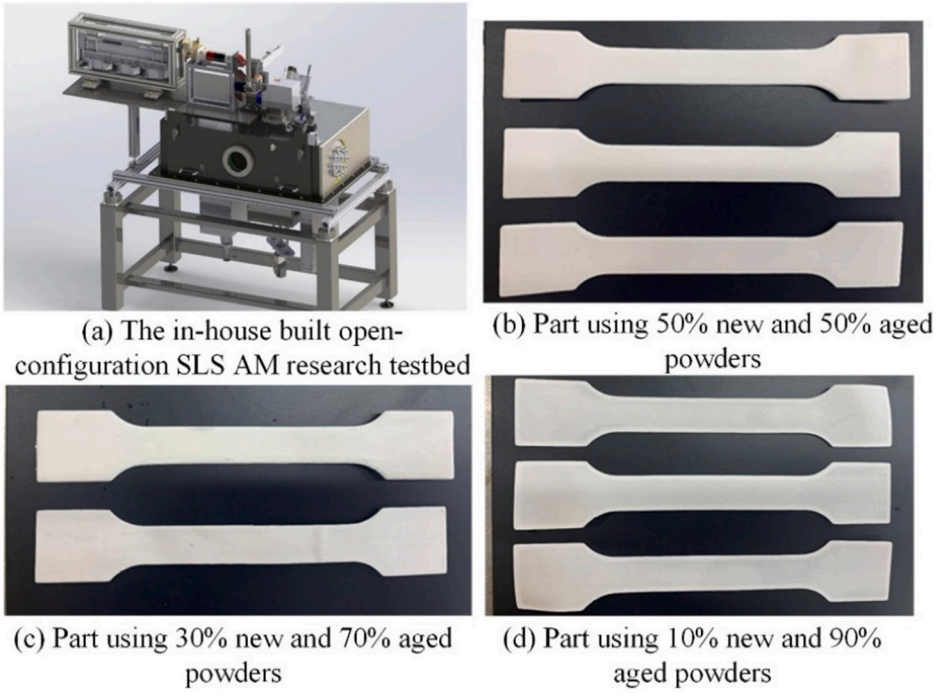

Fig. 2. SLS testbed and samples.

below $3/kg [19]. It is more economical to process the polyamide 12 powder residue into filaments for EAM or FDM rather than pellets for conventional plastics processing [19,20]. The common practice of reusing the polyamide 12 powder residue in SLS is to mix 50% new powders with 50% reclaimed powders from past experiments [13,19].

Besides, several research works dedicated to better understand the aging mechanisms of polyamide 12 in SLS. Diller et al. [21] built computational models at two complexity levels, a one-dimensional

Table 1
SLS printed samples using polyamide 12 powders, the calculated density, and oxidation time

Samples	Density/ g·cm^{-3}	Oxidation time/ seconds
Parts using 100% new powders	0.9	440; 480; 540; 720
Parts using 70% new and 30% aged powders	0.828	420; 720
Parts using 60% new and 40% aged powders	0.804	420; 720
Parts using 50% new and 50% aged powders	0.78	420; 720
Parts using 40% new and 60% aged powders	0.756	420, 720
Parts using 30% new and 70% aged powders	0.732	420; 720
Parts using 20% new and 80% aged powders	0.708	420; 720
Parts using 10% new and 90% aged powders	0.684	420; 720
Parts using 100% aged powders	0.66	440; 480; 540; 720

* Polyamide 12 new powders are purchased from EOS Corp. Polyamide 12 aged powders are reclaimed from standard SLS processes on an EOS P 390 machine.

Table 2
The elementary reaction constants for thermal oxidation of polyamide 12 at 160 °C [26,27,29].

Parameter	Value	Parameter	Value
k_2 (L·mol^{-1}·s^{-1})	10^8	k_{10} (L·mol^{-1}·s^{-1})	1.6×10^{11}
k_3 (L·mol^{-1}·s^{-1})	45.8	k_{11} (s^{-1})	2.0×10^8
k_6 (s^{-1})	8.0×10^{-4}	k_{12} (s^{-1})	3.4×10^8
k_7 (L·mol^{-1}·s^{-1})	6.0×10^{-3}	k_{13} (s^{-1})	2.2×10^9
k_8 (L·mol^{-1}·s^{-1})	8.0×10^{11}	γ_1 (%)	50
k_9 (L·mol^{-1}·s^{-1})	5.0×10^{11}	γ_2 (%)	50

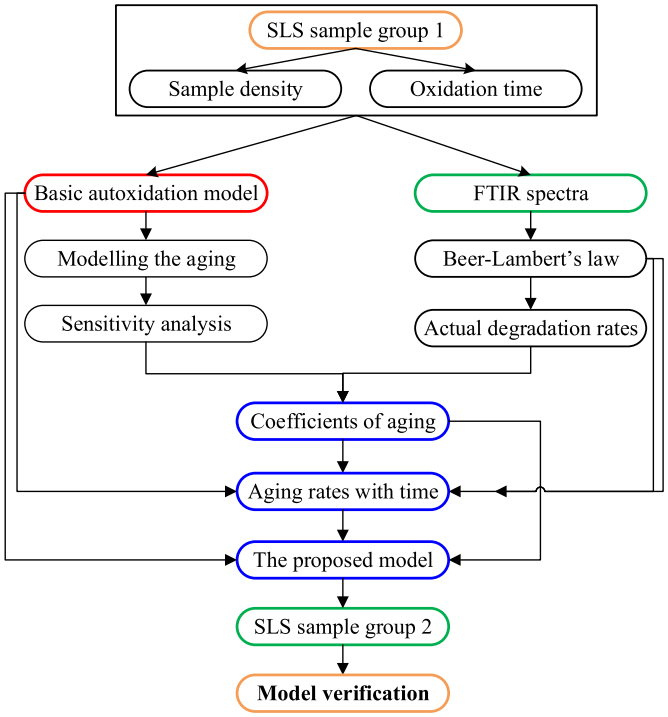

Fig. 3. Proposed procedures to build the kinetic model of polyamide 12 involving the coupled oxygen and laser-induced aging in SLS.

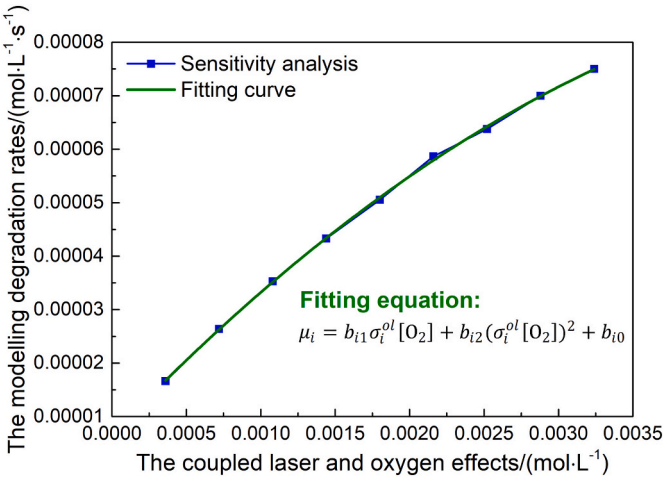

Fig. 4. Experimental relationship between μ_i and $\sigma_i^{ol}[O_2]$ for sample i.

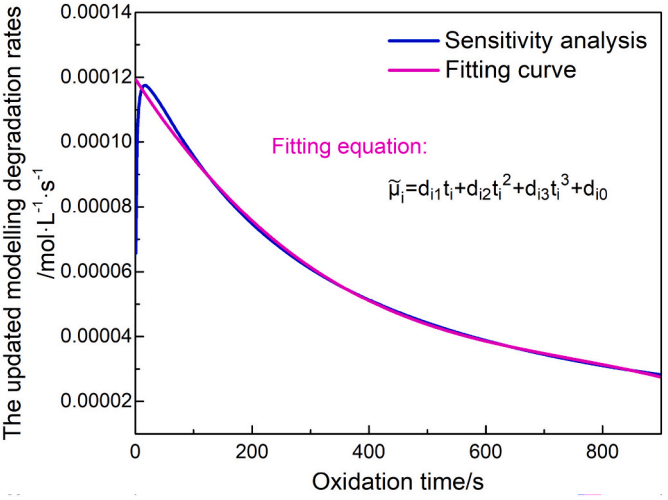

Fig. 5. Experimental relationship between $\tilde{\mu}_i$ and t_i for sample i.

Table 3
The elementary reaction constants for thermal oxidation of polyamide 12 between 90 and 150 °C [26,27,29].

Parameter	Value				
	90 °C	100 °C	120 °C	140 °C	150 °C
k_2 (L·mol^{-1}·s^{-1})	10^8	10^8	10^8	10^8	10^8
k_3 (L·mol^{-1}·s^{-1})	1.6	2.7	7.7	19.6	30.3
k_6 (s^{-1})	8.0×10^{-7}	2.2×10^{-6}	1.8×10^{-5}	1.6×10^{-4}	4.0×10^{-4}
k_7 (L·mol^{-1}·s^{-1})	4.0×10^{-5}	9.0×10^{-5}	5.0×10^{-4}	1.7×10^{-3}	3.5×10^{-3}
k_8 (L·mol^{-1}·s^{-1})	8.0×10^{11}	8.0×10^{11}	8.0×10^{11}	8.0×10^{11}	8.0×10^{11}
k_9 (L·mol^{-1}·s^{-1})	5.0×10^{11}	5.0×10^{11}	5.0×10^{11}	5.0×10^{11}	5.0×10^{11}
k_{10} (L·mol^{-1}·s^{-1})	8.0×10^9	2.6×10^{10}	6.0×10^{10}	5.0×10^{10}	9.5×10^{10}
k_{11} (s^{-1})	2.0×10^8	2.0×10^8	2.0×10^8	2.0×10^8	2.0×10^8
k_{12} (s^{-1})	3.4×10^8	3.4×10^8	3.4×10^8	3.4×10^8	3.4×10^8
k_{13} (s^{-1})	3.2×10^8	4.7×10^8	7.9×10^8	1.2×10^9	1.8×10^9
γ_1 (%)	100	95	80	55	55
γ_2 (%)	100	95	80	55	55

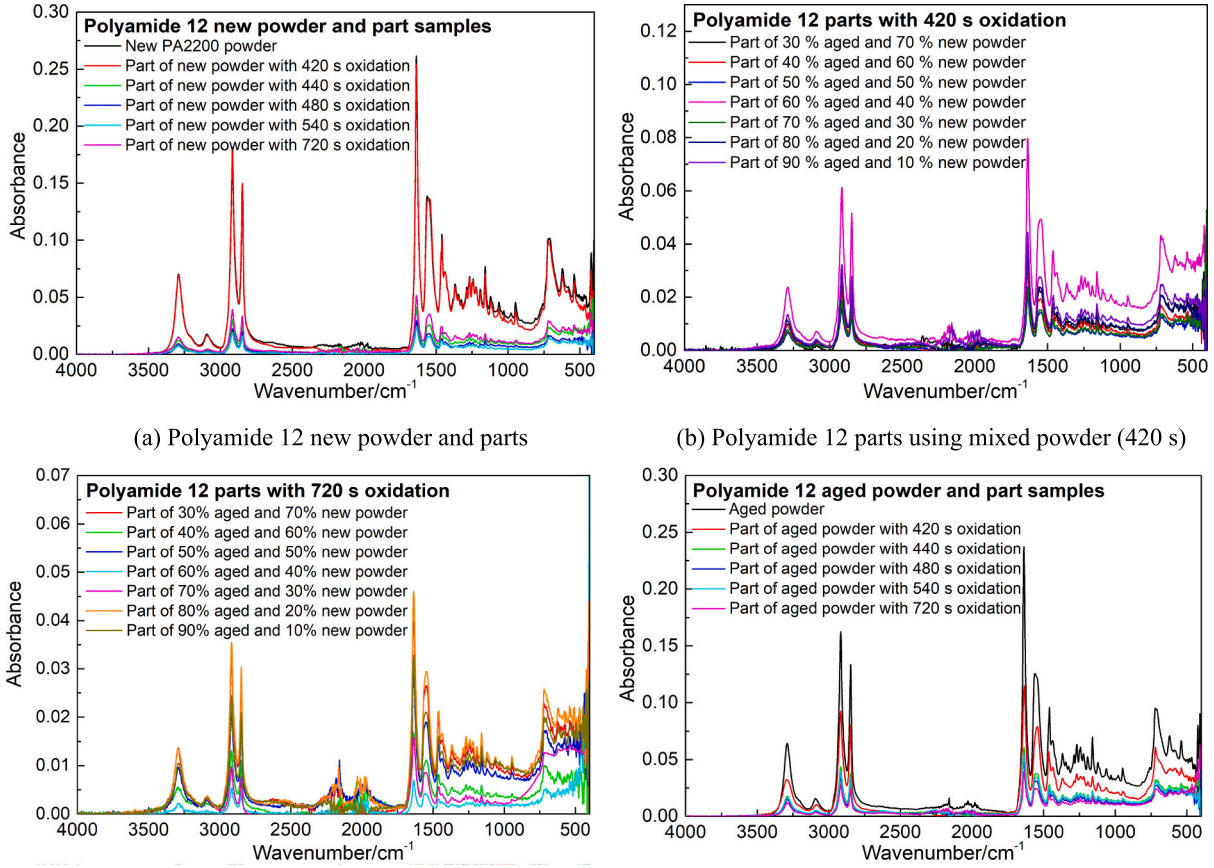

(a) Polyamide 12 new powder and parts

(b) Polyamide 12 parts using mixed powder (420 s)

(c) Polyamide 12 parts using mixed powder (720 s)

(d) Polyamide 12 aged powder and parts

Fig. 6. FTIR test results of different polyamide 12 powders and different 3D-printed part samples with different oxidation time.

model and a two-dimensional finite element model, to explore the influences of heat transfer on the aging of polyamide 12 in SLS. Yuan et al. [22] measured thermal conductivity of fresh and aged polyamide 12 powders to establish a baseline for thermal aging control in SLS. Dadbakhsh et al. [13] examined new and aged polyamide 12 powders along with their mixtures to identify the effect and mechanisms of in-process aging on material thermal and coalescence behaviors in SLS. Chen P et al. [12] investigated the aging mechanisms and microstructural evolution of polyamide 12 in SLS. Bernard et al. [23] performed thermogravimetric experiments with mass spectrometric analysis to obtain the kinetic parameters on the thermal degradation of polyamide 12 in SLS.

Heated and exposed to intensive laser radiations, the nature of material degradation in SLS involves coupled thermal and laser-induced oxidation reactions. Despite the previous works, the kinetics and the full modelling of polyamide 12 degradation in the complex SLS remain not well addressed. We propose a first-instance kinetic scheme considering both the oxygen and laser effects to model material degradation in SLS through multi-physics modelling and data-driven parametric identification. In this work, we conduct SLS printing experiments and calculate the actual polyamide 12 degradation rates through Fourier-transform infrared spectroscopy (FTIR) results and Beer-Lambert's law. By data-driven parameter identification of the actual SLS degradation rates into the oxidation model, we obtained the coefficients of actual coupled oxygen and laser effects in SLS. Through a further sensitivity analysis, we derive the relationship between the sample degradation rates and oxidation time. The proposed model can predict the degradation rates of materials using materials density and oxidation time. The new kinetic model applies to not only pure material but also mixed powders. Furthermore, using the proposed kinetic model, we identified the influences of the coupled oxygen, laser irradiation, and preheating on the rates of material degradation in the SLS of polyamide 12. The findings provide new knowledge of quantitative influences of the process parameters on material degradation and on approaches to reduce oxidation in SLS.

2. Method

Fig. 1 presents an overview of the proposed research approach. We discuss the details of each step in the following sections.

2.1. Oxidation model

2.1.1. Mechanism of thermal oxidation

Constituted of polymethylenic sequences and the amide group (-NHCO-), polyamide 12 has the following chemical structure:

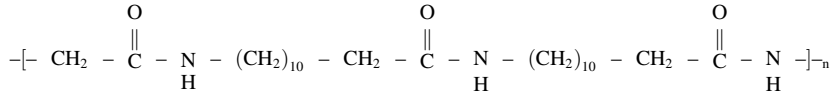

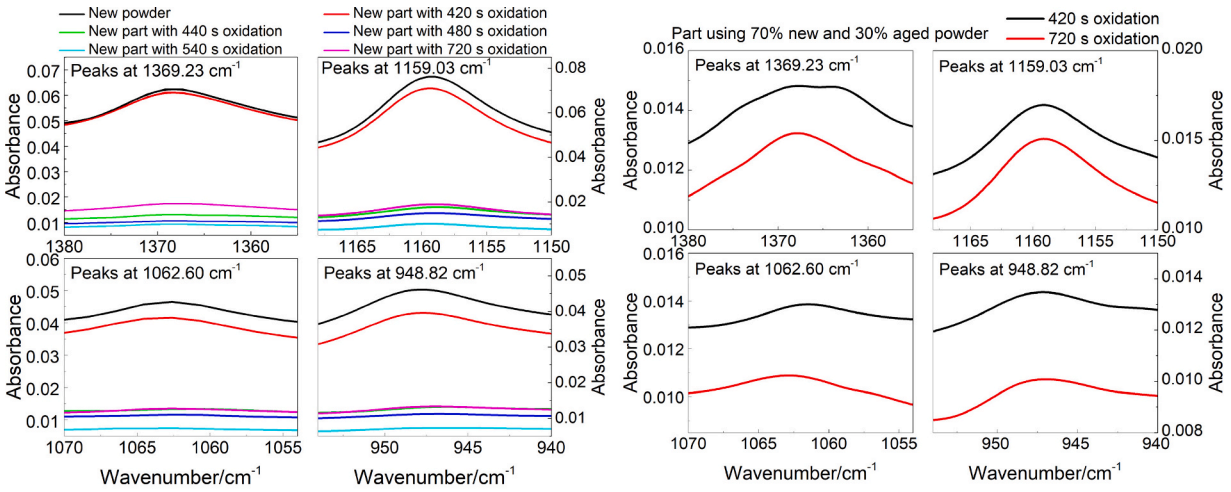

(a) New powder and parts using new powders

(b) Part using 70% new and 30% aged powders

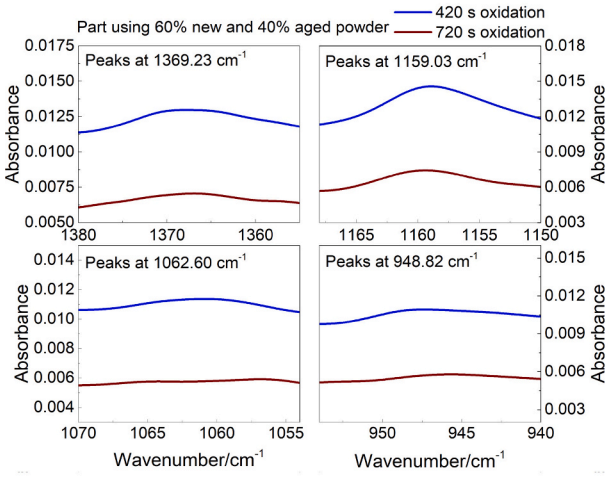

(c) Part using 60% new and 40% aged powders

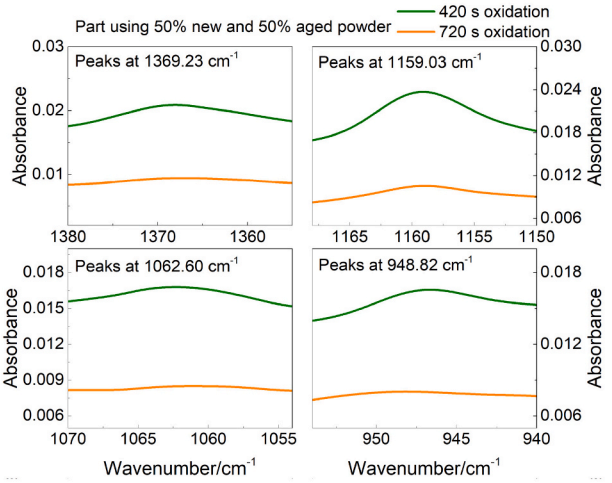

(d) Part using 50% new and 50% aged powders

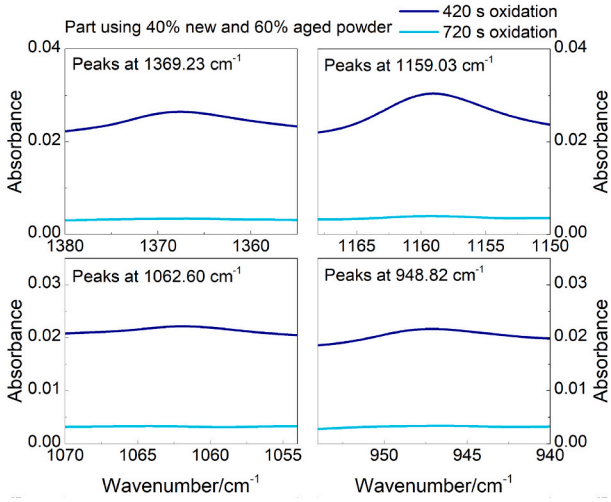

(e) Part using 40% new and 60% aged powders

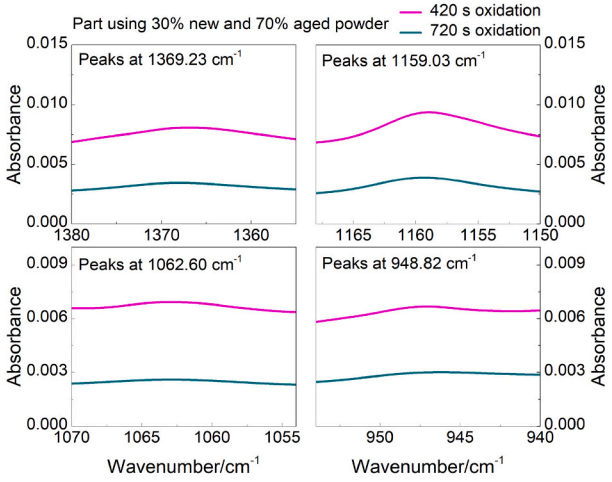

(f) Part using 30% new and 70% aged powders

Fig. 7. Comparison of FTIR peaks at the wavelengths of 1369.23, 1159.03, 1062.60, and 948.82 cm^{-1} when testing different polyamide 12 samples.

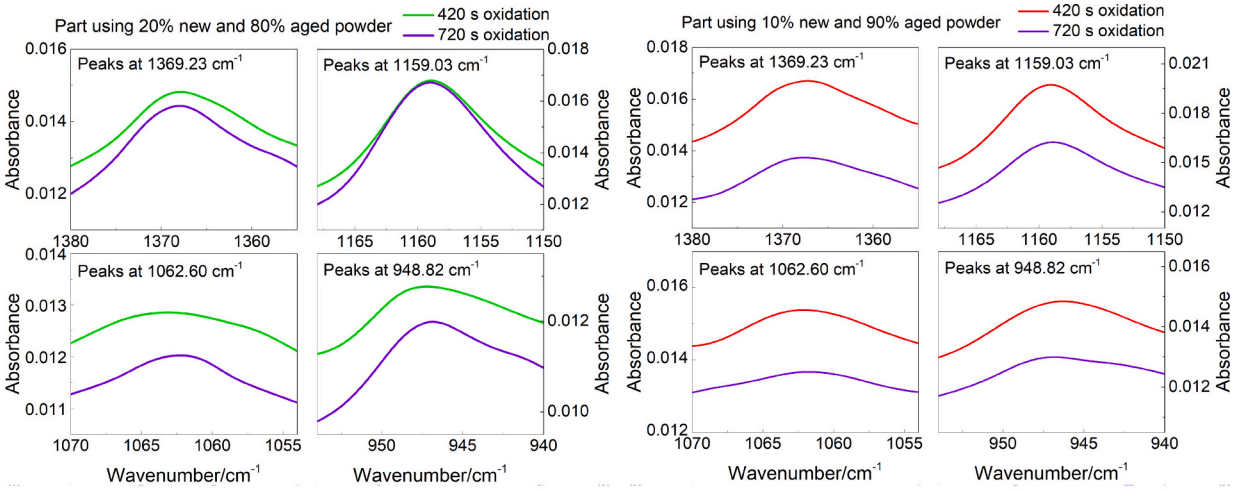

(g) Part using 20% new and 80% aged powders (h) Part using 10% new and 90% aged powders

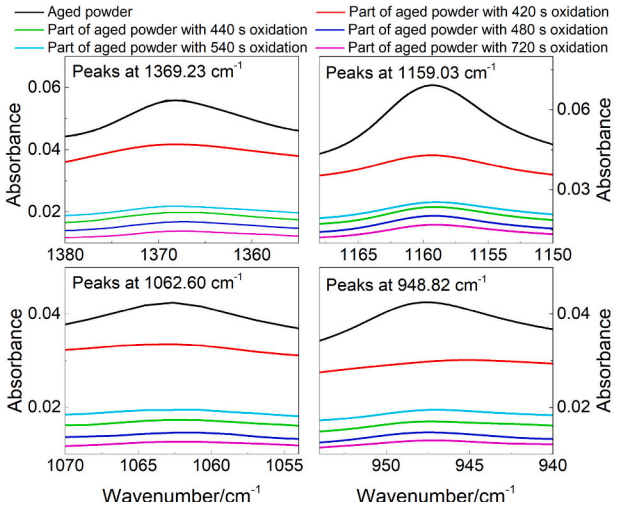

(i) Aged powder and parts using aged powders

Fig. 7. (*continued*).

From the basic autoxidation scheme of polymers [24,25], high temperatures initiate the thermal oxidation of polyamide 12 materials to form alkyl radicals P• (Eq. (1)). Incorporation of oxygen and abstraction of hydrogen atoms propagate oxidation of polyamide 12 [15]. In the propagation stage (Eqs. (2)–(3)), alkyl radicals P• combine with O_2 to form peroxy radicals PO_2•. PO_2• captures hydrogen atoms from polymer substrates to further produce hydroperoxides. Thermal decomposition of the hydroperoxide groups is the main mechanism of polymer oxidation below 200 °C. Such a process involves a unimolecular mode (Eq. (4)) and a bimolecular mode (Eq. (5)) [26,27]. Hydroxyl radicals PO•, alkoxy radicals HO•, and peroxy radicals PO_2• with polymer substrate rapidly interact and form two balance reactions (Eqs. (6)–(7)) [15]. This process also involves chain scission (S) and hydrogen abstraction.

$$\mathrm{PH\ (Polyamide\ 12)} \xrightarrow{k_1} \mathrm{P^{\cdot}} \tag{1}$$

$$\mathrm{P^{\cdot} + O_2} \xrightarrow{k_2} \mathrm{PO_2^{\cdot}} \tag{2}$$

$$\mathrm{PO_2^{\cdot} + PH} \xrightarrow{k_3} \mathrm{POOH + P^{\cdot}} \tag{3}$$

$$\mathrm{POOH} \xrightarrow{k_4} \mathrm{PO^{\cdot} + HO^{\cdot}} \tag{4}$$

$$\mathrm{2POOH} \xrightarrow{k_5} \mathrm{PO^{\cdot} + PO_2^{\cdot} + H_2O} \tag{5}$$

Balance reactions:

$$\mathrm{POOH} \xrightarrow{k_6} \mathrm{2P^{\cdot} + PNH_2^{\cdot} + PH = O + H_2O + S\ [-2PH,\ -CN]} \tag{6}$$

$$\mathrm{2POOH} \xrightarrow{k_7} \mathrm{P^{\cdot} + PO_2^{\cdot} + PNH_2 + PH = O + H_2O + S\ [-PH,\ -CN]} \tag{7}$$

Here, parameters k_i's are a series of elementary reaction constants of the thermal oxidation.

The termination reactions of alkyl radicals P• involve coupling or disproportionation (Eqs. (8)–(9)), where F and X denote double bonds and chain crosslinking (X), respectively. The termination reactions of peroxy radical pairs are ascribed as Eqs. (10)–(13). Peroxy radical pairs first react to form the transition cage $[PO^{\bullet\bullet}OP]_{cage}$ with oxygen. The transition cage further generates final products (e.g., POOP, $NH(P{=}O)_2$, and PNH_2) together with chain crosslinking (X) and scission (S).

$$\mathrm{P^{\cdot} + P} \xrightarrow{k_8} \gamma_1\mathrm{PP} + (1-\gamma_1)\mathrm{PH} + (1-\gamma_1)\mathrm{F} + \gamma_1\mathrm{X}\ [-(1-\gamma_1)\mathrm{PH}] \tag{8}$$

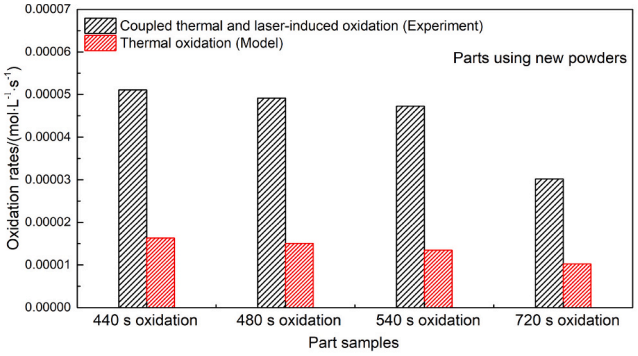

(a) Parts using new polyamide 12 powders

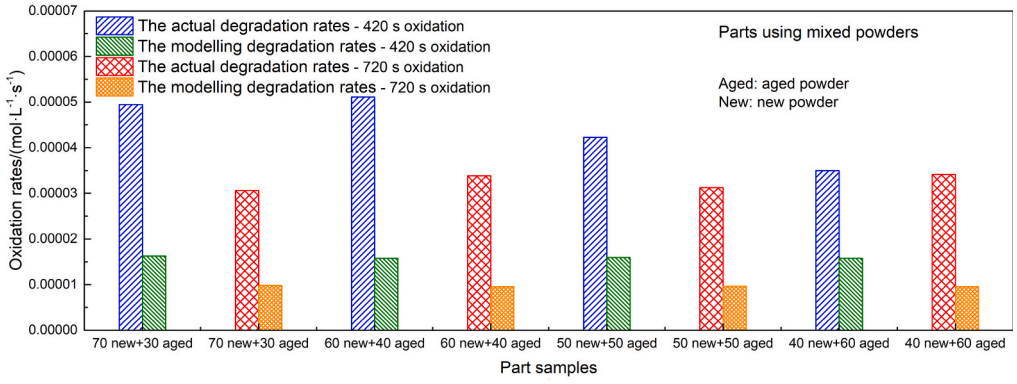

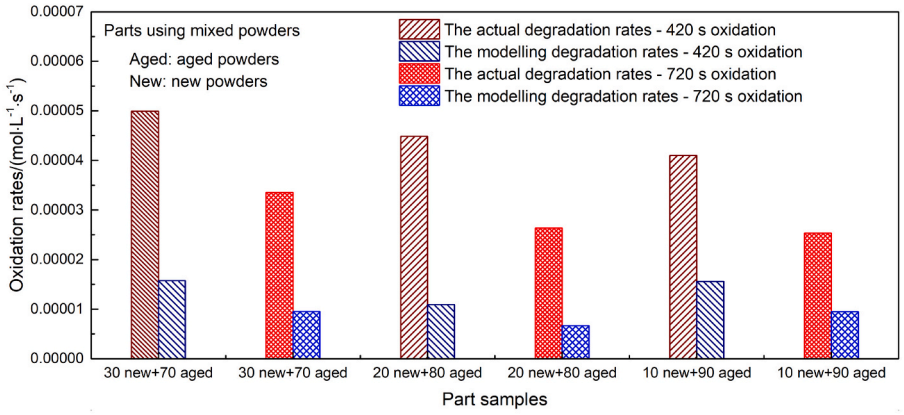

(b) Parts using mixed polyamide 12 powders

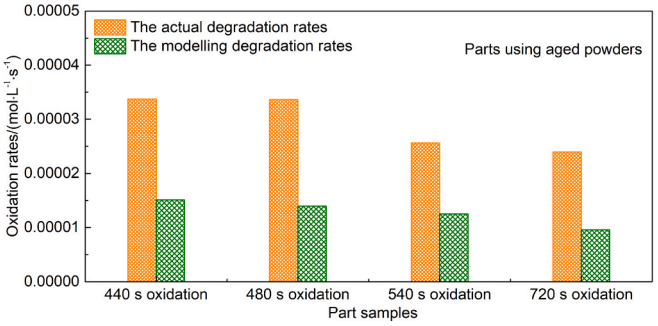

(c) Parts using aged polyamide 12 powders

Fig. 8. Comparisons between the modelling aging rates μ_i and the actual SLS aging rates η_i for different printed samples using polyamide 12 powders.

Table 4
SLS sample group 1.

Sample	Time of oxidation/seconds
Parts using 100% new powders	440, 480
Parts using 70% new and 30% aged powders	420
Parts using 60% new and 40% aged powders	420
Parts using 50% new and 50% aged powders	420
Parts using 40% new and 60% aged powders	720
Parts using 30% new and 70% aged powders	420
Parts using 20% new and 80% aged powders	420
Parts using 10% new and 90% aged powders	720
Parts using 100% aged powders	440, 480

$$P^{\cdot} + PO_2 \xrightarrow{k_9} \gamma_2 POOP + (1-\gamma_2)POOH + (1-\gamma_2)F + \gamma_2 X\,[-(1-\gamma_2)PH] \quad (9)$$

$$PO_2^{\cdot} + PO_2 \xrightarrow{k_{10}} [\dot{POOP}]_{cage} + O_2 \quad (10)$$

$$[\dot{POOP}]_{cage} \xrightarrow{k_{11}} POOP + X \quad (11)$$

$$[\dot{POOP}]_{cage} \xrightarrow{k_{12}} NH(P=O)_2 + PNH_2 + PH=O + S\,[-CN] \quad (12)$$

$$[\dot{POOP}]_{cage} \xrightarrow{k_{13}} 2P^{\cdot} + 2PNH_2 + 2PH=O + 2S\,[-2PH, -2CN] \quad (13)$$

2.1.2. Basic autoxidation model

The fundamental kinetics led to a basic model on thermal oxidation

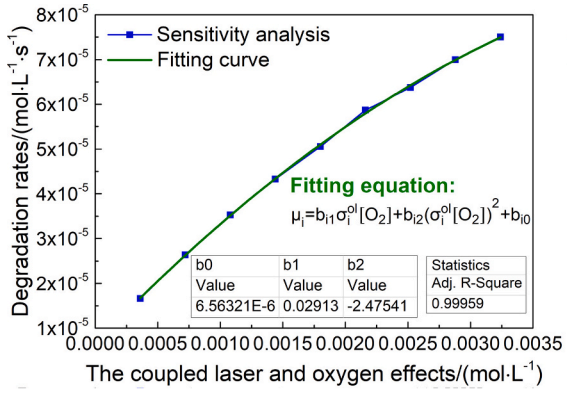

(a) 440 seconds of oxidation (part using new powders)

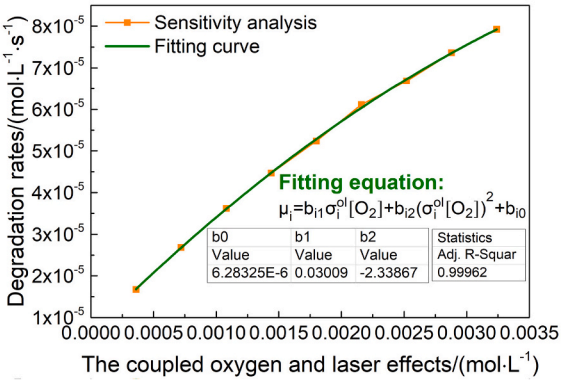

(b) 480 seconds of oxidation (part using new powders)

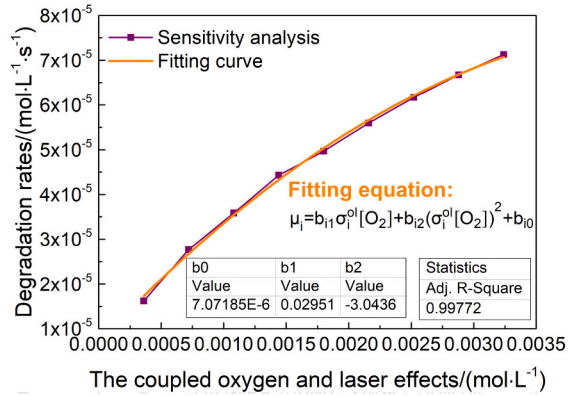

(c) 420 seconds of oxidation (part using 70% new powders)

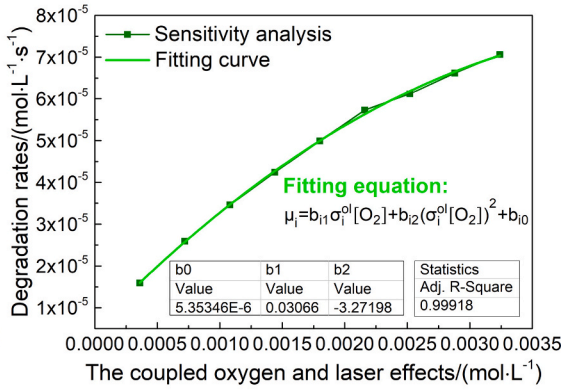

(d) 420 seconds of oxidation (part using 60% new powders)

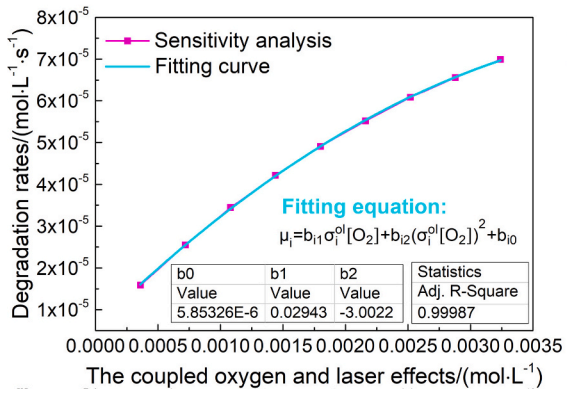

(e) 420 seconds of oxidation (part using 50% new powders)

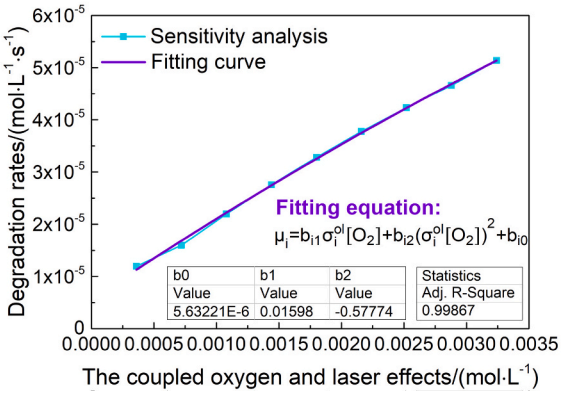

(f) 720 seconds of oxidation (part using 40% new powders)

Fig. 9. Sensitivity analysis and the fitting equations between μ_i and $\sigma_i^{ol}[O_2]$ to an R-squared second-order polynomial.

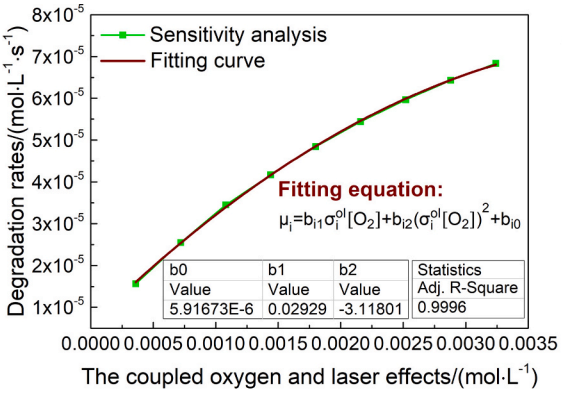

(g) 420 seconds of oxidation (part using 30% new powders)

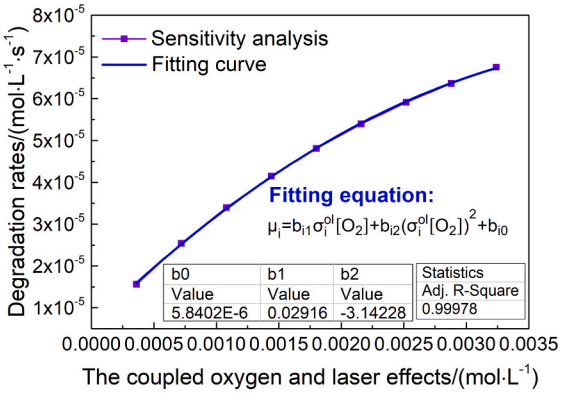

(h) 420 seconds of oxidation (part using 20% new powders)

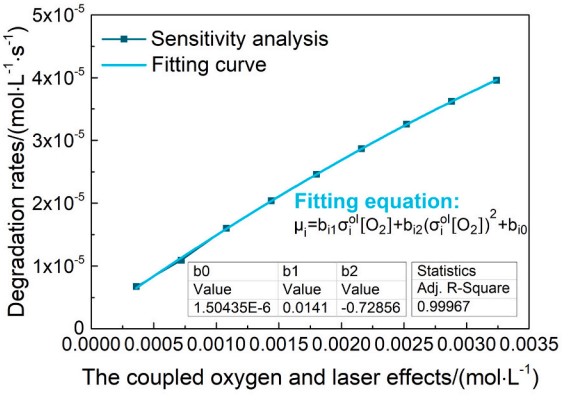

(i) 720 seconds of oxidation (part using 10% new powders)

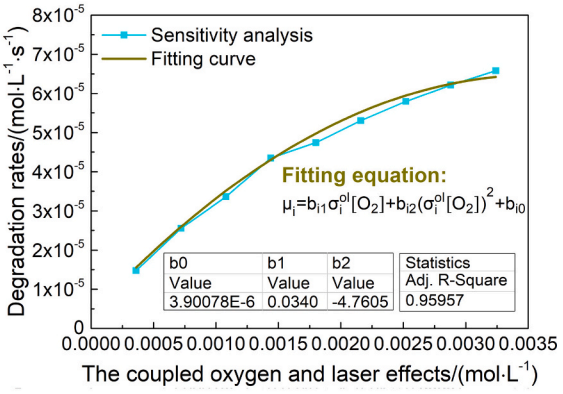

(j) 440 seconds of oxidation (part using aged powders)

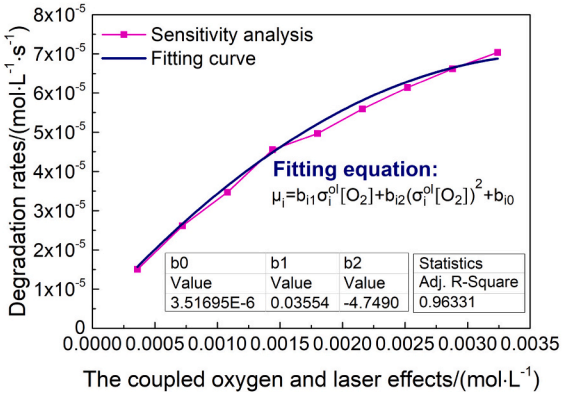

(k) 480 seconds of oxidation (part using aged powders)

Fig. 9. (*continued*).

of polyamide 12 materials, defined as the basic autoxidation model. The solution involves 5 main non-linear differential equations (Eqs. (14)–(18)) [15] indicating the derivatives of the compound concentrations with respect to time. For instance, the rate of concentration changes of [POOH] (Eq. (14)) equals the formation rates (POOH formed in Eqs. (3) and (9)) minus the consumption rates (POOH consumed in Eqs. (6) and (7)). We define the coefficient of oxygen effect as σ^o (Eqs. (15), (16), (19)), relating close to the oxygen concentrations [O_2]. σ^o equals 1 in the basic autoxidation model.

$$\frac{d[POOH]}{dt} = -k_6 f_{PH}[POOH] - 2k_7 f_{PH}[POOH]^2 + k_3[PH][PO_2^{\cdot}] + (1-\gamma_2)k_9 f_{PH}[P^{\cdot}][PO_2^{\cdot}] \quad (14)$$

$$\frac{d[P^{\cdot}]}{dt} = 2k_6 f_{PH}[POOH] + k_7 f_{PH}[POOH]^2 - k_2\sigma^o[O_2][P^{\cdot}] + k_3[PH][PO_2^{\cdot}] - 2k_8[P^{\cdot}]^2 - k_9 f_{PH}[P^{\cdot}][PO_2^{\cdot}] + 2k_{13} f_{PH}[\dot{POOP}]_{cage} \quad (15)$$

$$\frac{d[PO_2^{\cdot}]}{dt} = k_7 f_{PH}[POOH]^2 + k_2\sigma^o[O_2][P^{\cdot}] - k_3[PH][PO_2^{\cdot}] - k_9 f_{PH}[P^{\cdot}][PO_2^{\cdot}] - 2k_{10}[PO_2^{\cdot}]^2 \quad (16)$$

$$\frac{d[\dot{POOP}]_{cage}}{dt} = k_{10}[PO_2^{\cdot}]^2 - (k_{11}+k_{12}+k_{13}f_{PH})[\dot{POOP}]_{cage} \quad (17)$$

Table 5
The calculated coefficients of the coupled oxygen and laser effects, σ_{i-SLS}^{ol}, in the SLS process

Sample	Fitting curves between modelling degradation rates (μ_i) and the coupled oxygen and laser effects ($\sigma_i^{ol}[O_2]$)	The actual degradation rates in SLS η_i/ mol·L^{-1}·s^{-1}	The actual coupled laser and oxygen effects in SLS, $\sigma_{i-SLS}^{ol}[O_2]$/ mol·L^{-1}	Coefficients of the actual coupled laser and oxygen effects in SLS, σ_{i-SLS}^{ol}/ mol·L^{-1}
Fig. 9a	$\mu = 6.563 \times 10^{-6} + 0.029\sigma^{ol}[O_2] - 2.475(\sigma^{ol}[O_2])^2$	5.105×10^{-5}	1.804×10^{-3}	5.010
Fig. 9b	$\mu = 6.283 \times 10^{-6} + 0.030\sigma^{ol}[O_2] - 2.338(\sigma^{ol}[O_2])^2$	4.916×10^{-5}	1.632×10^{-3}	4.533
Fig. 9c	$\mu = 7.071 \times 10^{-6} + 0.029\sigma^{ol}[O_2] - 3.043(\sigma^{ol}[O_2])^2$	4.944×10^{-5}	1.753×10^{-3}	4.868
Fig. 9d	$\mu = 5.353 \times 10^{-6} + 0.031\sigma^{ol}[O_2] - 3.272(\sigma^{ol}[O_2])^2$	5.109×10^{-5}	1.861×10^{-3}	5.170
Fig. 9e	$\mu = 5.853 \times 10^{-6} + 0.029\sigma^{ol}[O_2] - 3.002(\sigma^{ol}[O_2])^2$	4.228×10^{-5}	1.453×10^{-3}	4.037
Fig. 9f	$\mu = 5.632 \times 10^{-6} + 0.016\sigma^{ol}[O_2] - 0.578(\sigma^{ol}[O_2])^2$	3.418×10^{-5}	1.919×10^{-3}	5.332
Fig. 9g	$\mu = 5.916 \times 10^{-6} + 0.029\sigma^{ol}[O_2] - 3.118(\sigma^{ol}[O_2])^2$	4.992×10^{-5}	1.878×10^{-3}	5.216
Fig. 9h	$\mu = 5.840 \times 10^{-6} + 0.029\sigma^{ol}[O_2] - 3.142(\sigma^{ol}[O_2])^2$	4.486×10^{-5}	1.622×10^{-3}	4.504
Fig. 9i	$\mu = 1.504 \times 10^{-6} + 0.014\sigma^{ol}[O_2] - 0.729(\sigma^{ol}[O_2])^2$	2.532×10^{-5}	1.622×10^{-3}	4.505
Fig. 9j	$\mu = 3.900 \times 10^{-6} + 0.034\sigma^{ol}[O_2] - 4.761(\sigma^{ol}[O_2])^2$	3.371×10^{-5}	1.022×10^{-3}	2.838
Fig. 9k	$\mu = 3.517 \times 10^{-6} + 0.036\sigma^{ol}[O_2] - 4.749(\sigma^{ol}[O_2])^2$	3.363×10^{-5}	9.740×10^{-4}	2.705

$$\frac{d[PH]}{dt} = -2k_6 f_{PH}[POOH] - k_7 f_{PH}[POOH]^2 - k_3[PH][PO_2^{\cdot}] - (1-\gamma_2)k_9 f_{PH}[P^{\cdot}][PO_2^{\cdot}] - 2k_{13} f_{PH}[\dot{POOP}]_{cage} \quad (18)$$

Here, f_{PH} is defined to avoid negative concentrations of substrate. $f_{PH} = [PH]/([PH] + \varepsilon)$ and $\varepsilon = 0.01$ [15]; the parameter itself does not significantly influence the oxidative kinetics.

From the mechanistic scheme in Section 2.1.1, we also obtain the concentration changes of the following reactants and products [15]:

$$\frac{d[O_2]_{Consumed}}{dt} = k_2\sigma^o[O_2][P^{\cdot}] - k_{10}[PO_2^{\cdot}]^2 \quad (19)$$

$$\frac{d[PNH_2]}{dt} = k_6 f_{PH}[POOH] + k_7 f_{PH}[POOH]^2 + (k_{12} + 2k_{13} f_{PH})[\dot{POOP}]_{cage} \quad (20)$$

$$\frac{d[PH=O]}{dt} = \frac{d[PNH_2]}{dt} \quad (21)$$

$$\frac{d[NH(P=O)_2]}{dt} = k_{12}[\dot{POOP}]_{cage} \quad (22)$$

$$\frac{d[C-N]}{dt} = -\frac{d[PNH_2]}{dt} \quad (23)$$

$$\frac{dS}{dt} = \frac{d[PNH_2]}{dt} \quad (24)$$

$$\frac{dX}{dt} = \gamma_1 k_8[P^{\cdot}]^2 + \gamma_2 k_9 f_{PH}[P^{\cdot}][PO_2^{\cdot}] + k_{11}[\dot{POOP}]_{cage} \quad (25)$$

Chain scission (S) occurs simultaneously with the oxidation-related signal diminishment near the wavelengths of 1369.23, 1159.03, 1062.60, and 948.82 cm^{-1} [12]. In the basic autoxidation model, we define the degree of chain scission (S) (Eq. (24)) occurring in unit time (s) as *the modelling aging rate* μ_i for polyamide 12 sample i.

$$\mu_i = \frac{\Delta S_i}{t_i} \quad (26)$$

where ΔS_i is the degree of chain scission in oxidation time t_i. We use Matlab ODE23s to solve the model when knowing the initial concentrations of the main component and the elementary reaction coefficients k_i. We will introduce the details of these parameters in Section 2.2.3.

At a specific temperature (e.g., a pre-heating temperature of the SLS machine, 160 °C), the elementary reaction coefficients k_i remain unchanged. However, the oxygen effect $\sigma^o[O_2]$ can vary significantly at a specific temperature when at different atmosphere, and largely affects the rates of material degradation. Stronger oxygen effects result in faster degradation rates. In SLS, the nature of material degradation involves the coupled oxygen and laser effects. The laser has even stronger effects than oxygen effects on material degradation. Thus, the coupled laser and oxygen effects are substantially more significant than the single oxygen effects on material degradation. However, it is difficult or impossible to get laser effects using the modelling-only approach. Through experimentation, we shall get the actual material degradation rates to derive *the coefficients of the coupled laser and oxygen effects*, referred to as σ_i^{ol}, through mapping experimental results to the modelling results. σ_i^{ol} shows the enhancement effects on material degradation from oxygen to the coupled laser and oxygen. $\sigma_i^{ol}[O_2]$ is the coupled laser and oxygen effects in SLS.

2.2. Experimentation

2.2.1. SLS printing using polyamide 12 powders

We sintered different polyamide 12 combinations. The SLS machine used is an in-house built open-configuration SLS AM research testbed with a 100 W Coherent GEM100A CO_2 laser and a Scanlab intelliSCAN 14 scanner (Fig. 2). The parameter settings used in the printing experiments are: 160 °C preheating, 3000 mm/s scanning speed, 18 W laser power, 0.3 mm scan spacing, and 150 μm layer thickness. Table 1 exhibits the 22 kinds of printed samples with calculated density and oxidation time (time in the chamber), i = 1, 2, …22. In detail, the oxidation time is the sum of the preheating, printing and the post-heating time. For part samples in this work, the preheating time is 5 min, and the printing time is 2 min. We change the post-heating time (20 s, 60 s, 120 s and 300 s) to obtain part samples with different oxidation time.

2.2.2. Measured material degradation rates

In the polyamide 12 FTIR spectra, the dramatically diminished signals of peaks near wavelengths of 1369.23, 1159.03, 1062.60, and 948.82 cm^{-1} indicate the oxidation of amide groups [12]. We conducted

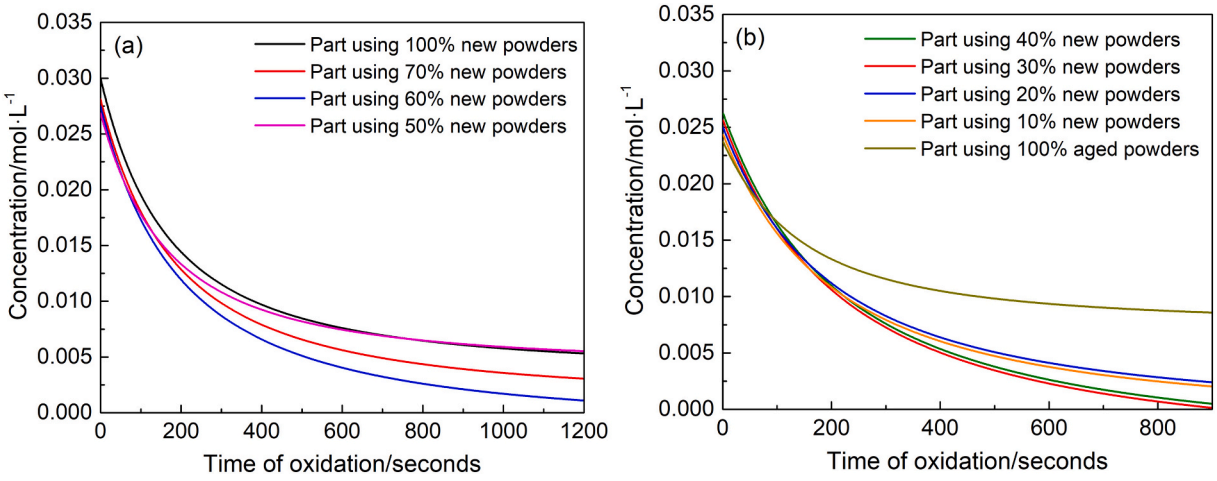

Fig. 10. Sensitivity analysis on concentration changes of the oxidative components as oxidation time t_i increases using the updated oxidation model.

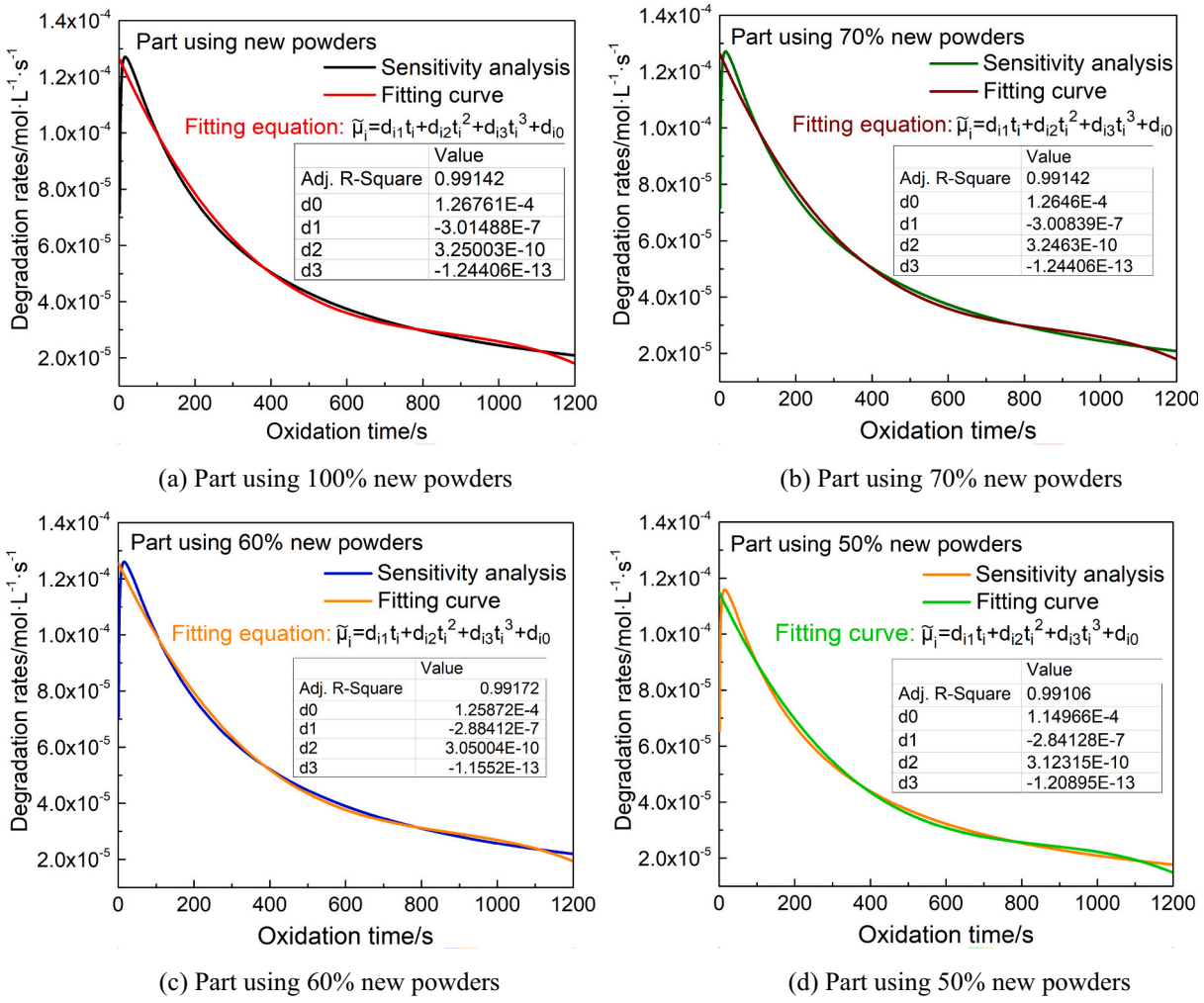

(a) Part using 100% new powders

(b) Part using 70% new powders

(c) Part using 60% new powders

(d) Part using 50% new powders

Fig. 11. Fitting equations between the updated modelling degradation rates $\tilde{\mu}_i$ and oxidation time t_i.

FTIR tests on the specimens in Table 1 as well as the pure polyamide 12 powder to examine the aging-related signals using a Nicolet Magna-IR 560 FTIR instrument (wavelength ranges: 6500 cm^{-1}-100 cm^{-1}, spectral resolution: 0.35 cm^{-1}). The FTIR of powder (new powder) serves as the benchmark against the degradation comparison. For specimen i, through the FTIR results and Beer-Lambert's law (Eq. (27)) [15], we calculated the concentrations of the four oxidation-related components Y_n ($n = 1,2,3,4$) (corresponding to peaks near 1369.23, 1159.03, 1062.60, and 948.82 cm^{-1}), respectively.

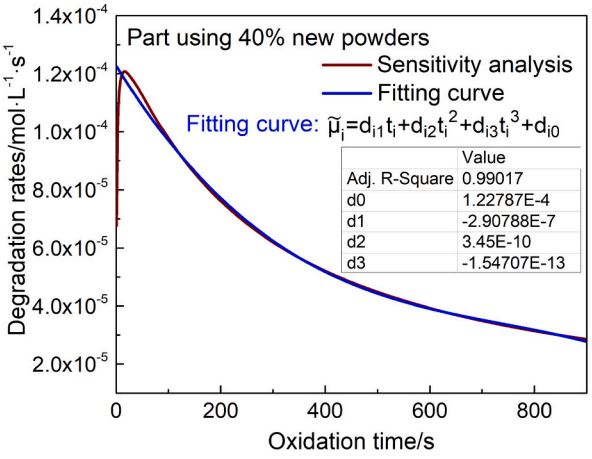

(e) Part using 40% new powders

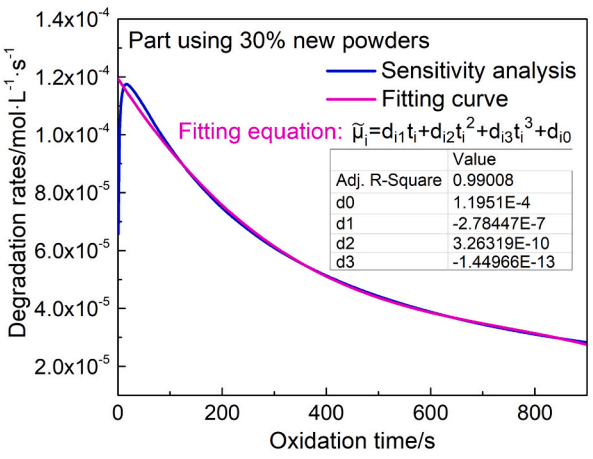

(f) Part using 30% new powders

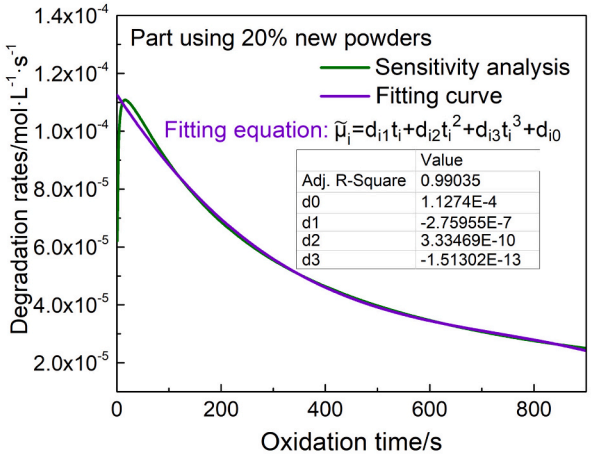

(g) Part using 20% new powders

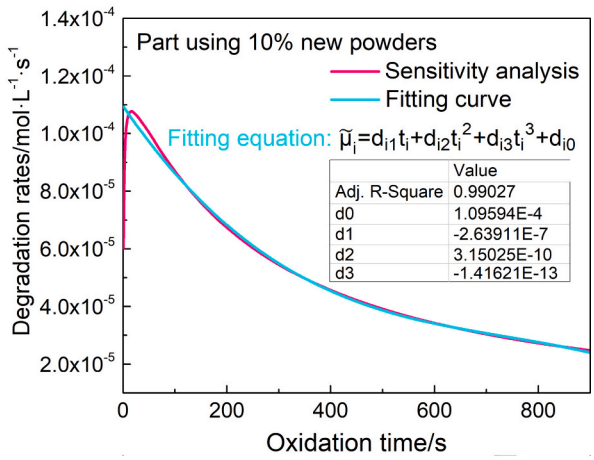

(h) Part using 10% new powders

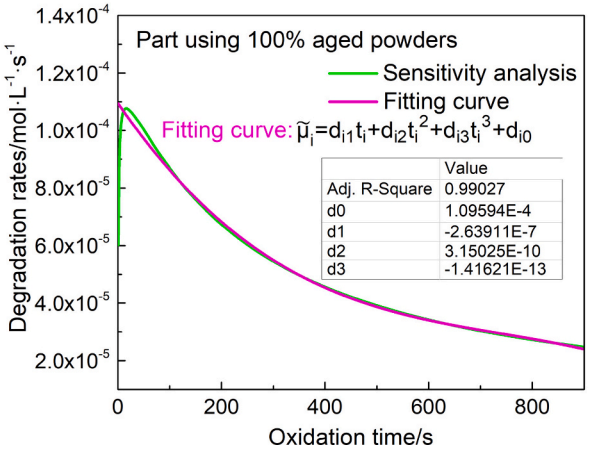

(i) Part using 100% aged powders

Fig. 11. (*continued*).

$$c_{Y_n}=\frac{\mathrm{Abs}(Y_n)}{\varepsilon_{Y_n}L_i}\quad(n=1,2,3,4) \tag{27}$$

where $\mathrm{Abs}(Y_n)$, ε_{Yn} and c_{Yn} are, respectively, the absorbance, the coefficient of molar absorptivity, and the concentrations of the chemical component Y_n; and L_i is the thickness of the tested sample i. We obtain the absorbances from FTIR results, and get the coefficients of molar absorptivity from the new powder (benchmark sample). For the new powder, we read the tested thickness and absorbances from FTIR, and calculate the molar concentrations using density and molar mass [28]. Then we get the coefficients of molar absorptivity using the Beer-Lambert's law [15], and insert these coefficients in Eq. (27) to calculate

Table 6
The coefficients of the actual coupled laser and oxygen effects in SLS, σ_{i-SLS}^{ol}, and the fitting equations between the updated modelling degradation rates $\widetilde{\mu}_i$ and oxidation time t_i.

Sample	σ_{i-SLS}^{ol}/ mol·L^{-1}	The fitting equations between the updated modelling degradation rates $\widetilde{\mu}_i$ and oxidation time t_i
Part using 100% new powders	4.772	$\widetilde{\mu} = 1.268 \times 10^{-4}$-3.015 $\times 10^{-7}$·t + 3.250 $\times 10^{-10}$·t^2–1.244 $\times 10^{-13}$·t^3
Part using 70% new powders	4.868	$\widetilde{\mu} = 1.265 \times 10^{-4}$-3.008 $\times 10^{-7}$·t + 3.246 $\times 10^{-10}$·t^2–1.244 $\times 10^{-13}$·t^3
Part using 60% new powders	5.170	$\widetilde{\mu} = 1.259 \times 10^{-4}$-2.884 $\times 10^{-7}$·t + 3.050 $\times 10^{-10}$·t^2–1.155 $\times 10^{-13}$·t^3
Part using 50% new powders	4.037	$\widetilde{\mu} = 1.149 \times 10^{-4}$-2.841 $\times 10^{-7}$·t + 3.123 $\times 10^{-10}$·t^2–1.209 $\times 10^{-13}$·t^3
Part using 40% new powders	5.332	$\widetilde{\mu} = 1.228 \times 10^{-4}$-2.908 $\times 10^{-7}$·t + 3.450 $\times 10^{-10}$·t^2–1.547 $\times 10^{-13}$·t^3
Part using 30% new powders	5.216	$\widetilde{\mu} = 1.195 \times 10^{-4}$-2.784 $\times 10^{-7}$·t + 3.263 $\times 10^{-10}$·t^2–1.449 $\times 10^{-13}$·t^3
Part using 20% new powders	4.504	$\widetilde{\mu} = 1.127 \times 10^{-4}$-2.759 $\times 10^{-7}$·t + 3.335 $\times 10^{-10}$·t^2–1.513 $\times 10^{-13}$·t^3
Part using 10% new powders	4.505	$\widetilde{\mu} = 1.096 \times 10^{-4}$-2.639 $\times 10^{-7}$·t + 3.150 $\times 10^{-10}$·t^2–1.416 $\times 10^{-13}$·t^3
Part using 100% aged powders	2.772	$\widetilde{\mu} = 1.096 \times 10^{-4}$-2.639 $\times 10^{-7}$·t + 3.150 $\times 10^{-10}$·t^2–1.416 $\times 10^{-13}$·t^3

Table 7
SLS sample group 2.

Sample	Oxidation time/seconds
Parts using 100% new powders	540, 720
Parts using 70% new and 30% aged powders	720
Parts using 60% new and 40% aged powders	720
Parts using 50% new and 50% aged powders	720
Parts using 40% new and 60% aged powders	420
Parts using 30% new and 70% aged powders	720
Parts using 20% new and 80% aged powders	720
Parts using 10% new and 90% aged powders	420
Parts using 100% aged powders	540, 720

concentrations of chemical component for part samples. We write Δc_{Yn} as the difference of c_{Yn} between the benchmarked powder materials and the 3D-printed samples. As there are four peaks for each specimen i, we write Δc_i (in mol/L) to denote the average of Δc_{Y1}, Δc_{Y2}, Δc_{Y3}, and Δc_{Y4} for specimen i. We define *the actual degradation rate* η_i (involving both oxygen and laser effects) as the average concentration changes of the oxidation-related components Δc_i in unit time (Eq. (28)), in mol/(L·s):

$$\eta_i = \frac{\Delta c_i}{t_i} \tag{28}$$

where i is the sample index in Table 1, and t_i is the associated oxidation time.

2.2.3. Comparisons between the actual SLS degradation η_i and the modelling aging rates μ_i

Specimen density and oxidation time in Table 1 are important parameters for the basic autoxidation model. Besides, the initial concentrations of reactants are necessary to run the model. For each specimen i, we get the initial concentrations of reactants, namely, POOH, PH and C − N,in the basic autoxidation model (Eqs. (14)–(25)) using the molar concentration formula

$$c_i^{reactant-R} = \frac{q_i}{M} \tag{29}$$

where $c_i^{reactant-R}$ (in molar/L) is the initial molar concentration of reactant R (POOH, PH or C − N) in specimen i; q_i (in g/cm^3) is the density of specimen i; M (in g/mol) is the molar mass of polyamide 12. In the basic autoxidation, the initial concentrations of P$^{\bullet}$, $PO_2^{\bullet}$, $[PO^{\bullet\bullet}OP]_{cage}$, $[O_2]_{Consumed}$, PNH_2, PH = O, NH(P = O)$_2$, S, and X are zero because they are intermediate products. The oxygen concentration, $[O_2]$, is 3.6 × 10^{-4} mol·L^{-1} [15] in the air atmosphere. Table 2 lists the elementary reaction coefficients for thermal oxidation of polyamide 12 at 160 °C [26,27,29]. Inserting the above parameters in the basic autoxidation model, we get *the modelling aging rate* μ_i for sample i, and compare the result to *the actual degradation rate* η_i.

2.3. Kinetic model of polyamide 12 aging in SLS considering the coupled oxygen and laser effects

Fig. 3 shows the main proposed procedures to build the kinetic model of polyamide 12 aging involving the coupled oxygen and laser effects in SLS.

We separated the printed SLS specimens in Table 1 into two sample groups (SLS sample groups 1 and 2). Each group contains SLS samples with different polyamide 12 combinations. The objective is to ensure that the method can derive *the coefficient of the coupled oxygen and laser effects*, σ_i^{ol}, for different polyamide 12 combinations. For samples i in group 1, we performed sensitivity analysis on *the modelling degradation rates* μ_i as the coupled laser and oxygen effects $\sigma_i^{ol}[O_2]$ changes, using the basic autoxidation model. Fig. 4 presents the relationship between μ_i and $\sigma_i^{ol}[O_2]$ for sample i.

The experimental data suggest a second-order relationship between μ_i and $\sigma_i^{ol}[O_2]$ in the tested operation zone. We thus propose the following second-order correlation mapping

$$\mu_i = b_{i1}\sigma_i^{ol}[O_2] + b_{i2}\left(\sigma_i^{ol}[O_2]\right)^2 + b_{i0} \tag{30}$$

where b_{i0}, b_{i1}, and b_{i2} are constants for sample i. We will perform parameter identification with R-squared regression and a full model verification in Section 3. When *the modelling degradation rate* μ_i equals *the actual degradation rate* η_i (Section 2.2.2), the corresponding $\sigma_i^{ol}[O_2]$ represents the actual coupled laser and oxygen effects in SLS, defined as $\sigma_{i-SLS}^{ol}[O_2]$.

Replacing σ^o with σ_{i-SLS}^{ol} in the basic autoxidation model, we obtain an updated oxidation model of polyamide 12 in SLS. In this model, we define the material degradation rates as *the updated modelling degradation rates* $\widetilde{\mu}_i$. We utilize the updated model to conduct sensitivity analysis on $\widetilde{\mu}_i$ and the specimen oxidation time t_i. Fig. 5 shows the experimentally identified relationship between $\widetilde{\mu}_i$ and t_i for sample i.

After the initial transient, the relationship between $\widetilde{\mu}_i$ and t_i fits an R-squared cubic polynomial, defined as Eq. (31).

$$\widetilde{\mu}_i = d_{i1}t_i + d_{i2}t_i^2 + d_{i3}t_i^3 + d_{i0} \tag{31}$$

where d_{i0}, d_{i1}, d_{i2} and d_{i3} are constants.

The proposed kinetic model contains the basic autoxidation model, *the coefficient of the actual coupled laser and oxygen effects in SLS*, and the relationships between *the updated modelling degradation rates* $\widetilde{\mu}_i$ and specimen oxidation time t_i. To verify the proposed kinetic model, we apply it to the SLS sample group 2 to compare *the updated modelling aging rates* $\widetilde{\mu}_i$ and *the actual degradation rates* η_i.

2.4. Characteristics of the updated modelling degradation rates $\widetilde{\mu}_i$

The actual coupled laser and oxygen effects in SLS, $\sigma_{i-SLS}^{ol}[O_2]$, and the preheating temperature are predominant parameters in SLS affecting the material degradation rates. To understand the process further, we use the proposed kinetic model to identify the influences of $\sigma_{i-SLS}^{ol}[O_2]$ and preheating temperatures (Tables 2 and 3) on *the updated modelling degradation rates*, $\widetilde{\mu}_i$. These results will be analyzed in Section 3.3.

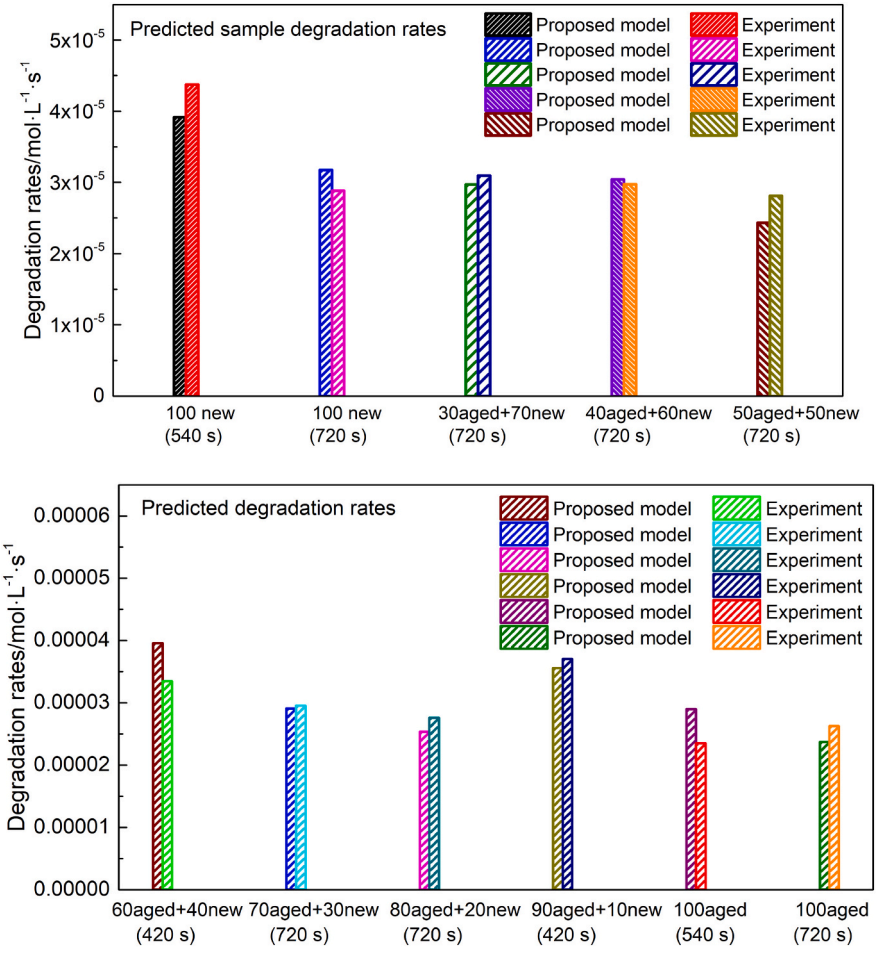

Fig. 12. The comparisons between the predicted degradation rates $\tilde{\mu}_i$ and the actual SLS degradation rates η_i of the SLS sample group 2 (Parts using polyamide 12 powders of different combinations).

Table 8
Comparisons between the actual SLS degradation rates η_i, the modelling degradation rates μ_i from the basic autoxidation model, and the updated modelling degradation $\tilde{\mu}_i$ from the proposed kinetic model.

Sample	The actual SLS degradation rates η_i/ mol·L^{-1}·s^{-1}	The basic autoxidation model		The proposed kinetic model	
		Degradation rates μ_i/ mol·L^{-1}·s^{-1}	Deviation/ %	Degradation rates $\tilde{\mu}_i$/mol·L^{-1}·s^{-1}	Deviation/ %
Part/100% new powder/ 540 s	4.726×10^{-5}	1.347×10^{-5}	71.505	3.913×10^{-5}	17.177
Part/100% new powder/ 720 s	3.021×10^{-5}	1.023×10^{-5}	66.129	3.174×10^{-5}	5.054
Part/70% new powder/720 s	3.065×10^{-5}	9.819×10^{-6}	67.964	2.971×10^{-5}	3.065
Part/60% new powder/720 s	3.386×10^{-5}	9.538×10^{-6}	71.832	2.971×10^{-5}	10.156
Part/50% new powder/720 s	3.128×10^{-5}	9.648×10^{-6}	69.162	2.432×10^{-5}	22.260
Part/40% new powder/420 s	3.4974×10^{-5}	1.577×10^{-5}	54.894	3.954×10^{-5}	13.058
Part/30% new powder/720 s	3.354×10^{-5}	9.545×10^{-6}	71.542	2.907×10^{-5}	13.319
Part/20% new powder/720 s	2.634×10^{-5}	6.678×10^{-6}	74.647	2.533×10^{-5}	3.823
Part/10% new powder/420 s	4.100×10^{-5}	1.560×10^{-5}	61.943	3.554×10^{-5}	13.311
Part/100% aged powder/ 540 s	2.560×10^{-5}	1.253×10^{-5}	51.069	2.894×10^{-5}	13.044
Part/100% aged powder/ 720 s	2.395×10^{-5}	9.568×10^{-6}	60.045	2.372×10^{-5}	0.936

3. Results and discussions

3.1. Comparisons between the modelling aging μ_i and the actual SLS aging rates η_i

As introduced in Section 2.2.3, we run the basic autoxidation model and get the modelling degradation rates μ_i for each specimen i in Table 1, presented in the following section. As for the actual degradation, Fig. 6 exhibits the FTIR results of the SLS samples in Table 1, which we shall now extrapolate into measured degradation rates η_i. The horizontal axis is the wavenumber, and the vertical axis is the absorbance. Our focus here is to get the absorbance differences of oxidation-related

Table 9
The decreasing $\sigma_{i-SLS}{}^{ol}[O_2]$

Sample	The actual coupled laser and oxygen effects in SLS, $\sigma_{i-SLS}{}^{ol}[O_2]$/mol·L^{-1}	$\sigma_{i-SLS}{}^{ol}[O_2]$/2	$\sigma_{i-SLS}{}^{ol}[O_2]$/5	$\sigma_{i-SLS}{}^{ol}[O_2]$/10	$\sigma_{i-SLS}{}^{ol}[O_2]$/20	$\sigma_{i-SLS}{}^{ol}[O_2]$/50	$\sigma_{i-SLS}{}^{ol}[O_2]$/100
		Unit: mol·L^{-1}					
Part using 100% new powders	1.718×10^{-3}	8.589×10^{-4}	3.435×10^{-4}	1.718×10^{-4}	8.589×10^{-5}	3.435×10^{-5}	1.718×10^{-5}
Part using 50% new powders	1.453×10^{-3}	7.267×10^{-4}	2.907×10^{-4}	1.453×10^{-4}	7.267×10^{-5}	2.907×10^{-5}	1.453×10^{-5}
Part using 100% aged powders	9.978×10^{-4}	4.989×10^{-4}	1.996×10^{-4}	9.978×10^{-5}	4.989×10^{-5}	1.996×10^{-5}	9.978×10^{-6}

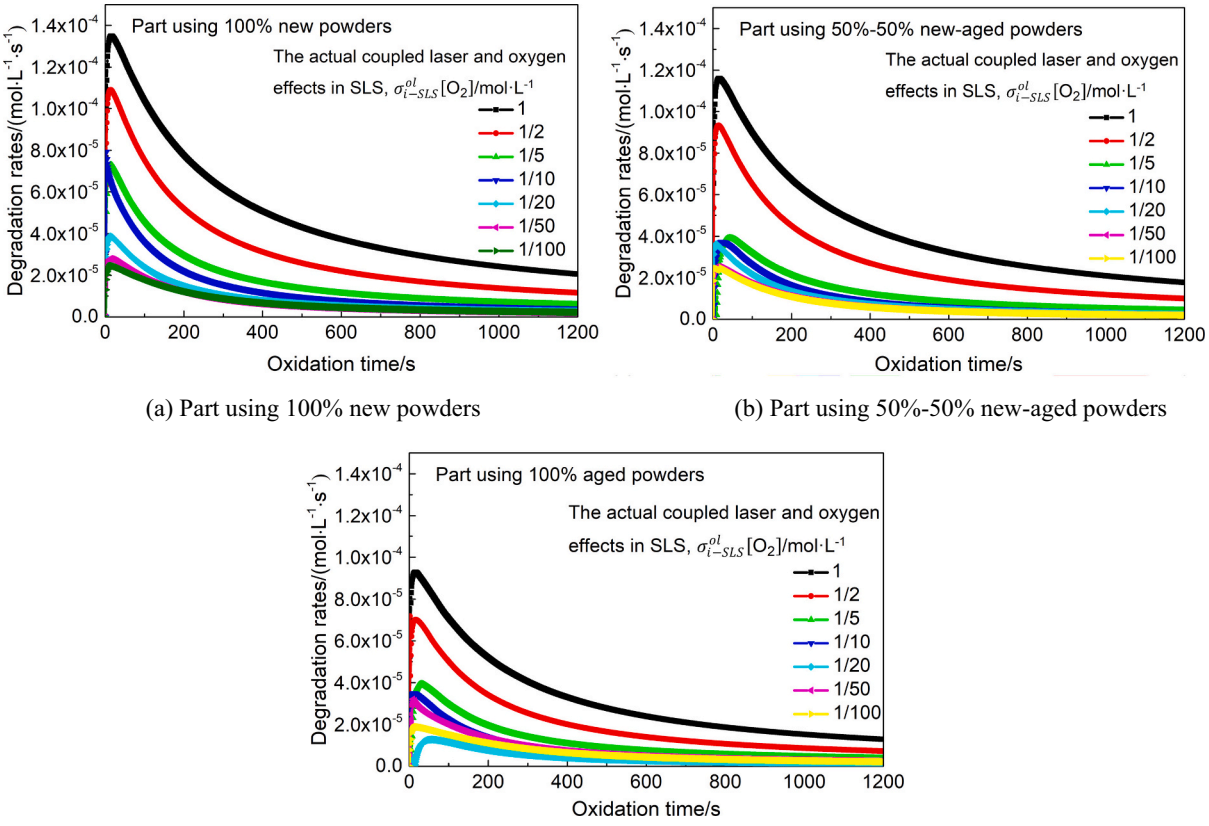

(a) Part using 100% new powders

(b) Part using 50%-50% new-aged powders

(c) Part using 100% aged powders

Fig. 13. Curves between the updated modelling degradation rates $\tilde{\mu}_i$ and oxidation time t_i with decreasing $\sigma_{i-SLS}{}^{ol}[O_2]$ for different part samples

Table 10
The increasing $\sigma_{i-SLS}{}^{ol}[O_2]$

Sample	The actual coupled laser and oxygen effects in SLS, $\sigma_{i-SLS}{}^{ol}[O_2]$ /mol·L^{-1}	$\sigma_{i-SLS}{}^{ol}[O_2] \times 2$	$\sigma_{i-SLS}{}^{ol}[O_2] \times 5$	$\sigma_{i-SLS}{}^{ol}[O_2] \times 10$	$\sigma_{i-SLS}{}^{ol}[O_2] \times 20$	$\sigma_{i-SLS}{}^{ol}[O_2] \times 50$	$\sigma_{i-SLS}{}^{ol}[O_2] \times 100$
		Unit: mol·L^{-1}					
Part using 100% new powders	1.718×10^{-3}	3.435×10^{-3}	8.589×10^{-3}	1.718×10^{-2}	3.435×10^{-2}	8.589×10^{-2}	1.718×10^{-1}
Part using 50% new powders	1.453×10^{-3}	2.907×10^{-3}	7.267×10^{-3}	1.453×10^{-2}	2.907×10^{-2}	7.267×10^{-2}	1.453×10^{-1}
Part using 100% aged powders	9.978×10^{-4}	1.996×10^{-3}	4.989×10^{-3}	9.978×10^{-3}	1.996×10^{-2}	4.989×10^{-2}	9.978×10^{-2}

wavelengths at 1369.23, 1159.03, 1062.60, and 948.82 cm^{-1}. Then using the Beer-Lambert's law [15], we can calculate the concentrations of the oxidation-related components for each sample. The differences of the concentrations between different samples represent the different oxidation states.

Fig. 7 compares FTIR curves of SLS samples at the oxidation-related wavelengths of 1369.23, 1159.03, 1062.60, and 948.82 cm^{-1}. The diminishment or disappearance of peaks at oxidation-related components indicates the material degradation and oxidization (Fig. 7a and i). The peaks decrease more when the aging time increases (Fig. 7b, c, d, e, f, g, and h). As introduced in Section 2.2.2, we calculated the concentration changes (mol·L^{-1}) of oxidation-related components for each

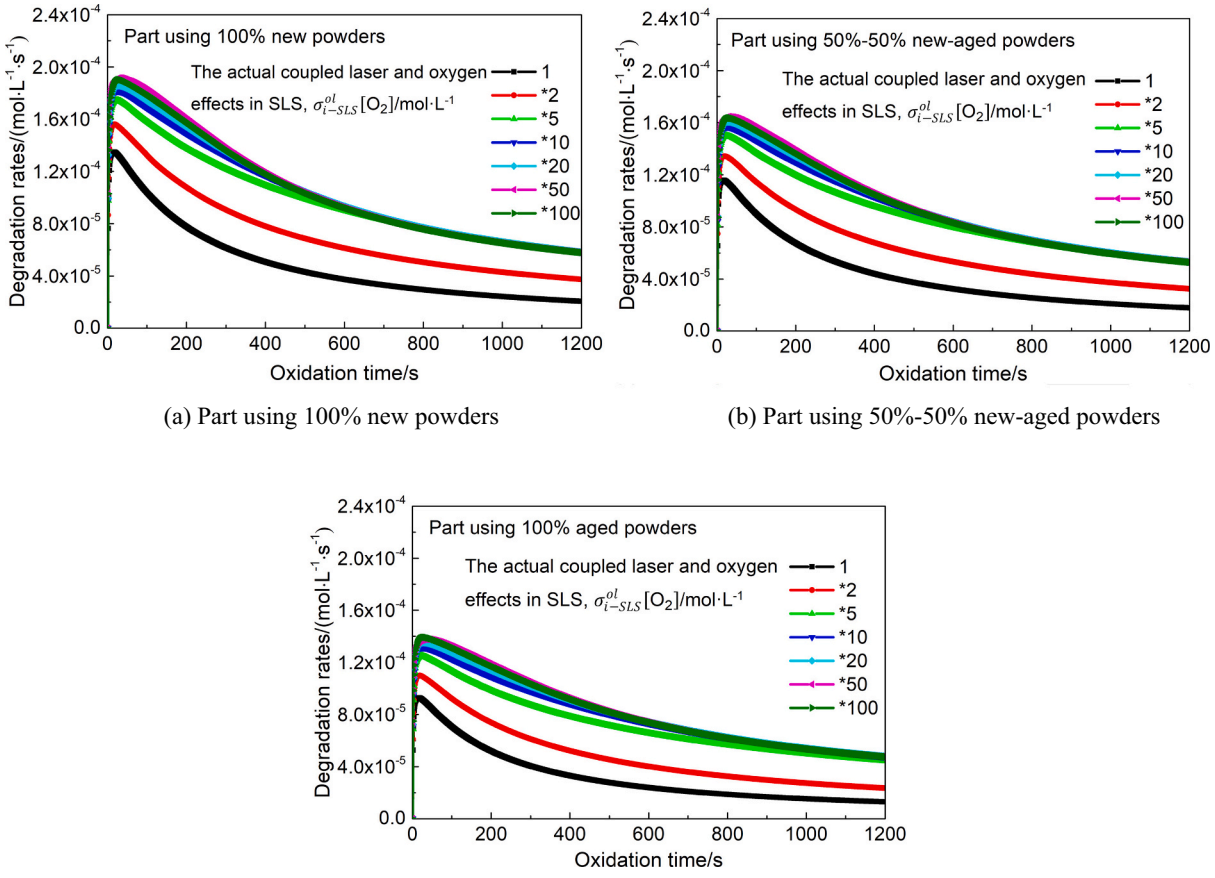

(a) Part using 100% new powders

(b) Part using 50%-50% new-aged powders

(c) Part using 100% aged powders

Fig. 14. Curves between the updated modelling degradation rates $\tilde{\mu}_i$ and oxidation time t_i with increasing $\sigma_{i-SLS}{}^{ol}[O_2]$ for different part samples.

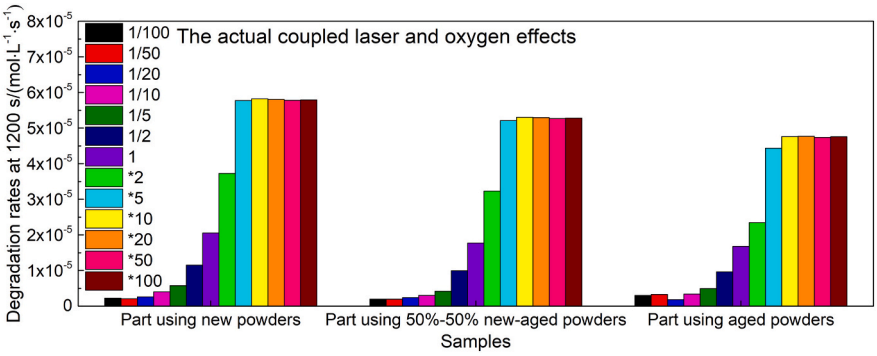

Fig. 15. Comparisons of $\tilde{\mu}_i$ at 1200 s for different samples to compare material degradation rates at a more stable state

sample during specific aging durations, and further obtained the actual degradation rates η_i in mol·L^{-1}·s^{-1} using the Eqs. (27)–(28).

Fig. 8 compares the modelling degradation rates μ_i and the actual degradation rates η_i. Nontrivial but unsurprising, the actual degradation rates of polyamide 12 are much larger than the modelling degradation rates. This phenomenon exists in all samples, including those using pure new polyamide 12 powders (Fig. 8a), new-aged mixed powders (Fig. 8b), and pure aged powders (Fig. 8c). This core finding indicates that the coupled oxygen and laser age the material much faster than the case with oxygen only. It is thus necessary and important to build the kinetic model of polyamide 12 aging in SLS considering the coupled oxygen and laser effects.

3.2. Building the kinetic model of polyamide 12 aging in SLS considering the coupled oxygen and laser effects

3.2.1. Determining the coefficients of the actual coupled laser and oxygen effects in SLS, $\sigma_{i-SLS}{}^{ol}$

Table 4 shows the selected SLS sample group 1 and the associated time of oxidation. After performing the sensitivity analysis using the basic autoxidation model, we conducted curve fitting between the modelling degradation rates μ_i and the coupled laser and oxygen effects $\sigma_i^{ol}[O_2]$ to an R-squared second-order polynomial (Eq. (30)). Fig. 9 exhibits the results of sensitivity analysis and the fitting equations.

In each fitting equation, letting the modelling degradation rates, μ_i, equal to the actual degradation rates η_i, we obtain the actual coupled

Table 11
Comparisons of $\widetilde{\mu}_i$@1200 s between the original $\sigma_{i-SLS}^{ol}[O_2]$ and the decreased/increased $\sigma_{i-SLS}^{ol}[O_2]$ for different samples

Samples	Part using new powders	Part using 50%–50% new-aged powders	Part using aged powders
The decreasing $\sigma_{i-SLS}^{ol}[O_2]$	Percentages of $\widetilde{\mu}_i$@1200 s decreasing when $\sigma_{i-SLS}^{ol}[O_2]$ decreasing		
$\sigma_{i-SLS}^{ol}[O_2]/100$	89.02	88.77	81.9
$\sigma_{i-SLS}^{ol}[O_2]/50$	89.73	88.77	80.53
$\sigma_{i-SLS}^{ol}[O_2]/20$	87.13	86.45	88.89
$\sigma_{i-SLS}^{ol}[O_2]/10$	80.38	82.86	79.73
$\sigma_{i-SLS}^{ol}[O_2]/5$	71.96	76.27	70.54
$\sigma_{i-SLS}^{ol}[O_2]/2$	43.83	43.82	42.4
The increasing $\sigma_{i-SLS}^{ol}[O_2]$	Percentages of $\widetilde{\mu}_i$@1200 s increasing when $\sigma_{i-SLS}^{ol}[O_2]$ increasing		
$\sigma_{i-SLS}^{ol}[O_2] \times 2$	81.41	82.13	39.87
$\sigma_{i-SLS}^{ol}[O_2] \times 5$	180.91	193.45	164.06
$\sigma_{i-SLS}^{ol}[O_2] \times 10$	183.34	198.76	183.6
$\sigma_{i-SLS}^{ol}[O_2] \times 20$	182.53	198.23	184.14
$\sigma_{i-SLS}^{ol}[O_2] \times 20$	181.13	196.76	182.41
$\sigma_{i-SLS}^{ol}[O_2] \times 100$	181.78	197.35	183.42

laser and oxygen effects in SLS, $\sigma_{i-SLS}^{ol}[O_2]$, and the coefficients of σ_{i-SLS}^{ol} (Table 5). Here, we obtain the updated oxidation model, including the basic autoxidation model and σ_{i-SLS}^{ol}. The values of σ_{i-SLS}^{ol} indicate that the coupled laser and oxygen effects are about 4 times more than the case with only oxygen ($\sigma^o = 1$), and *the laser effects are on average 4.4 times stronger than oxygen effects on polyamide 12 degradation.*

3.2.2. Determining the relationship between the updated modelling degradation rates $\widetilde{\mu}_i$ and oxidation time t_i

This subsection identifies the relationships between the updated modelling degradation rates $\widetilde{\mu}_i$ and oxidation time t_i using the updated oxidation model. First, we conducted a sensitivity analysis on concentration changes of oxidative components as oxidation time t_i increases (Fig. 10). The observation is that the sample using 100% aged powders has the slowest rates of concentration changes when $t_i > 100$ s. This is largely due to that the aged powders develop a lot of oxidized components from the thermal history.

We divided the concentration changes by oxidation time t_i to get degradation curves, and fit the curves to a series of cubic-polynomial (Eq. (31)). Fig. 11 shows the fitting equations between the updated modelling degradation rates $\widetilde{\mu}_i$ and oxidation time t_i. In the sensitivity analysis curve, the model output $\widetilde{\mu}_i$ goes up quickly from zero to the maximum and then goes down within seconds. The reason is that a strong thermal impetus initiates and simultaneously accelerates the degradation reaction at a time close to zero. At this stage, the impetus dominantly controls the reaction and continuously increases the degradation rates until arriving at the maximum point. However, when the reaction runs normally, the basic parameters, e.g., initial concentrations of components, elementary reaction coefficients, laser and oxygen effects, take control of the reaction. At this stage, the influences of the initiation impetus on degradation rates diminish rapidly and disappear gradually.

3.2.3. The proposed kinetic model

For different polyamide 12 powder combinations, Table 6 lists the coefficients of the actual coupled laser and oxygen effects in SLS, σ_{i-SLS}^{ol}, and the fitting equations between the updated modelling degradation

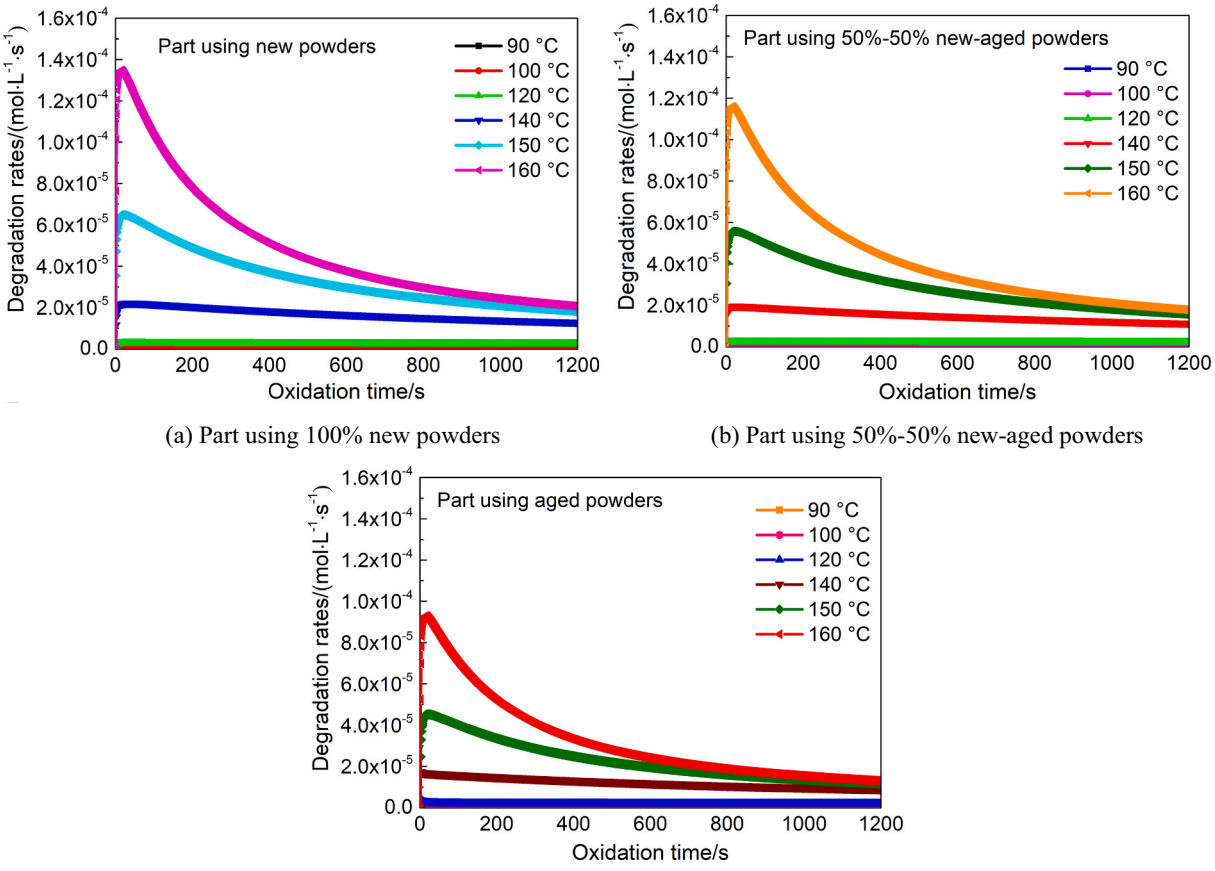

(a) Part using 100% new powders

(b) Part using 50%-50% new-aged powders

(c) Part using 100% aged powders

Fig. 16. Curves between the updated modelling degradation rates $\widetilde{\mu}_i$ and oxidation time t_i with different preheating temperatures for different part samples

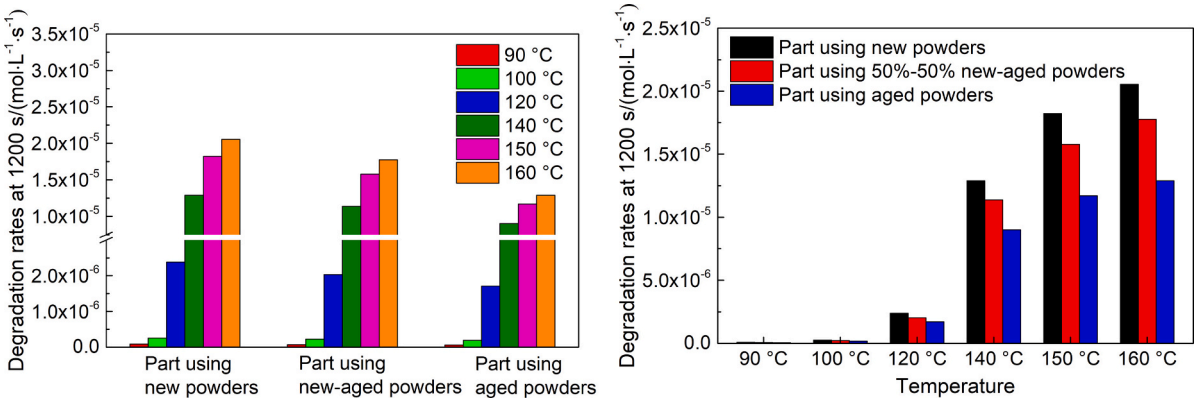

(a) Samples with different preheating temperatures (b) Preheating temperatures for different samples

Fig. 17. Comparisons of $\widetilde{\mu}_i$ at 1200 s ($\widetilde{\mu}_i$@1200 s) between (a) Samples with different preheating temperatures, and (b) Preheating temperatures for different samples

rates $\widetilde{\mu}_i$ and oxidation time t_i. The proposed kinetic scheme of polyamide 12 aging in SLS considering the coupled oxygen and laser effects includes the basic autoxidation model, $\sigma_{i-SLS}{}^{ol}$ and fitting equations between $\widetilde{\mu}_i$ and t_i. From there, we can predict the sample degradation in SLS through powder combination and oxidation time.

Inserting the modelling related parameters of SLS sample group 2 (Table 7) into the proposed kinetic model, we predicted the degradation rates of these samples. Fig. 12 compares the predicted degradation $\widetilde{\mu}_i$ using the proposed kinetic model and the measured actual SLS degradation η_i of sample group 2. Small deviations between the predicted $\widetilde{\mu}_i$ and the actual degradation results η_i exist. Fig. 12 presents average deviations of 9.43% between $\widetilde{\mu}_i$ and η_i, respectively, exhibiting a substantial improvement compared to the results in Fig. 8. The proposed kinetic model is capable to predict the SLS degradation rates of polyamide 12 accurately.

3.2.4. Discussions

Table 8 presents the actual SLS degradation rates η_i from experimentation, the modelling degradation rates μ_i from the basic autoxidation model, and the updated modelling degradation rates $\widetilde{\mu}_i$ from the proposed kinetic model. The modelling degradation rates μ_i have large deviations compared to the actual SLS degradation rates η_i, while the updated modelling degradation rates $\widetilde{\mu}_i$ are close to η_i. The predicted degradations $\widetilde{\mu}_i$ from the proposed kinetic model match on average 89.53% with the actual SLS degradation rates η_i, in contrast to a 34.48% accuracy from a basic autoxidation model.

3.3. Characteristics of the updated modelling degradation rates $\widetilde{\mu}_i$

3.3.1. Influences of the coupled laser and oxygen effects on $\widetilde{\mu}_i$

3.3.1.1. Degradation characteristics in presence of decreasing oxidations. To identify the degradation trend here, we reduce $\sigma_{i-SLS}{}^{ol}[O_2]$ for different part samples in Table 9. Inserting the $\sigma_{i-SLS}{}^{ol}[O_2]$ into the proposed kinetic model, we obtained $\widetilde{\mu}_i - t_i$ curves between the updated modelling degradation rates $\widetilde{\mu}_i$ and oxidation time t_i (Fig. 13). Fig. 13a, b, and c is the results for, respectively, SLS 3D-printed part using 100% new powders, part using 50%–50% new-aged powders, and part using 100% aged powders. The $\widetilde{\mu}_i - t_i$ curves in different colors point out the nonlinear relationship between $\sigma_{i-SLS}{}^{ol}[O_2]$ and the degradation rate. The black curves in Fig. 13a–c are the benchmark $\widetilde{\mu}_i - t_i$ curves with the original $\sigma_{i-SLS}{}^{ol}[O_2]$.

For different samples in Fig. 13, when $\sigma_{i-SLS}{}^{ol}[O_2]$ reduces, the updated modelling degradation rates increase from zero to the maximum quickly, then decrease with time. For a specific sample (e.g., Fig. 13a, the new-SLS part), the maximum of $\widetilde{\mu}_i$ drops as $\sigma_{i-SLS}{}^{ol}[O_2]$ decreases. The new-SLS part (Fig. 13a) always has the largest degradation rate, while the aged-SLS part (Fig. 13c) has the smallest $\widetilde{\mu}_i$. For the mixed (Fig. 13b) and aged-SLS parts (Fig. 13c), curves with $\sigma_{i-SLS}{}^{ol}[O_2]/2$ (7.267×10^{-4} mol/L for mixed and 4.989×10^{-4} mol/L for aged) and $\sigma_{i-SLS}{}^{ol}[O_2]/5$ (2.907×10^{-4} mol/L for mixed and 1.996×10^{-4} mol/L for aged) result in a large drop of $\widetilde{\mu}_i$ compared to the benchmark $\widetilde{\mu}_i - t_i$ curves, especially at the peak degradation points. However, further curves (curves with $\sigma_{i-SLS}{}^{ol}[O_2]/10$, $\sigma_{i-SLS}{}^{ol}[O_2]/20$, and $\sigma_{i-SLS}{}^{ol}[O_2]/100$) show small changes in comparison to the curve with $\sigma_{i-SLS}{}^{ol}[O_2]/5$. After about 1200 s of oxidation ($t_i = 1200$ s), the rates of degradation all approach the steady state. This convergence is much faster when the oxidation effect is reduced. In addition, when reusing powders, degradation significantly slows down when oxidation is reduced by a factor of 5, and remains afterwards (Figure 13bc).

3.3.1.2. Degradation characteristics in presence of increasing oxidations. Table 10 presents the designed experiments with increasing $\sigma_{i-SLS}{}^{ol}[O_2]$ for different part samples. Applying the increasing $\sigma_{i-SLS}{}^{ol}[O_2]$ to the proposed kinetic model, we obtain the $\widetilde{\mu}_i - t_i$ curves between the updated modelling degradation rates and oxidation time (Fig. 14). Fig. 14a, b, and c is respectively for SLS 3D-printed part using 100% new powders, part using 50%–50% new-aged powders, and part using 100% aged powders. The curves in different colors represent differently increased $\sigma_{i-SLS}{}^{ol}[O_2]$. The black curves in Fig. 14a–c are the benchmark $\widetilde{\mu}_i - t_i$ curves with the original $\sigma_{i-SLS}{}^{ol}[O_2]$.

In Fig. 14, $\widetilde{\mu}_i$ increases from zero to the maximum quickly, then decreases with time. For any specific sample (e.g., Fig. 14a, the new-SLS part), the maximum of $\widetilde{\mu}_i$ rises as $\sigma_{i-SLS}{}^{ol}[O_2]$ increases. Having the same increasing degree for $\sigma_{i-SLS}{}^{ol}[O_2]$ (e.g., $\sigma_{i-SLS}{}^{ol}[O_2] \times 10$), the new-SLS part always has the largest $\widetilde{\mu}_i$, while the aged-SLS part has the smallest $\widetilde{\mu}_i$. For new, mixed, and aged-SLS parts, curves with $\sigma_{i-SLS}{}^{ol}[O_2] \times 2$ and $\sigma_{i-SLS}{}^{ol}[O_2] \times 5$ lead to obvious increases of $\widetilde{\mu}_i$. However, the other curves (curves with $\sigma_{i-SLS}{}^{ol}[O_2] \times 10$, $\sigma_{i-SLS}{}^{ol}[O_2] \times 20$, $\sigma_{i-SLS}{}^{ol}[O_2] \times 50$, $\sigma_{i-SLS}{}^{ol}[O_2] \times 100$) differ little compared to the curve with $\sigma_{i-SLS}{}^{ol}[O_2] \times 5$. The result indicates that further increasing $\sigma_{i-SLS}{}^{ol}[O_2]$ does not influence $\widetilde{\mu}_i$ significantly. Till 1200 s, all the curves are at or close to reaching the steady state.

3.3.1.3. Comparisons. Fig. 15 compares $\widetilde{\mu}_i$ at 1200 s for different samples to reveal material degradation rates at the steady state. In Fig. 15, the purple bars are the benchmark $\widetilde{\mu}_i$@1200 s data with the original $\sigma_{i-SLS}{}^{ol}[O_2]$. When $\sigma_{i-SLS}{}^{ol}[O_2]$ decreases (increases), the $\widetilde{\mu}_i$@1200 s decreases (increases) quickly first. Further decreasing (increasing) $\sigma_{i-SLS}{}^{ol}[O_2]$ has little effects on $\widetilde{\mu}_i$@1200 s.

Table 11 compares $\widetilde{\mu}_i$@1200 s between the original $\sigma_{i-SLS}{}^{ol}[O_2]$ and the decreased/increased $\sigma_{i-SLS}{}^{ol}[O_2]$ for different samples. In contrast to

the case with the original $\sigma_{i-SLS}^{ol}[O_2]$, $\widetilde{\mu}_i$@1200 s with $\sigma_{i-SLS}^{ol}[O_2]/100$ decreased by, respectively, 89.02%, 88.77%, and 81.90% for the new, mixed and aged-SLS parts. On the other hand, $\widetilde{\mu}_i$@1200 s with $\sigma_{i-SLS}^{ol}[O_2] \times 100$ increased by, respectively, 181.78%, 197.35%, and 183.42% for the new, mixed and aged-SLS parts.

3.3.2. Influences of the preheating temperature on $\widetilde{\mu}_i$

Fig. 16 presents the curves ($\widetilde{\mu}_i - t_i$ curves) between the updated modelling degradation rates $\widetilde{\mu}_i$ and oxidation time t_i with different preheating temperatures for (a) Part using 100% new powders, (b) Part using 50%–50% new-aged powders, and (c) Part using 100% aged powders. In Fig. 16a–c, the decreased preheating temperatures lower the $\widetilde{\mu}_i - t_i$ curves. When at the same temperature (e.g., 150 °C, 140 °C), the new-SLS part has the largest $\widetilde{\mu}_i$ (Fig. 16a), while the aged-SLS part has the smallest $\widetilde{\mu}_i$ (Fig. 16c). As the preheating temperature decreases, the peaks in the $\widetilde{\mu}_i - t_i$ curves diminish (from 160 °C to 140 °C) and disappear gradually (from 120 °C to 90 °C). Therefore, the peaks in the $\widetilde{\mu}_i - t_i$ curves are likely caused by the high temperature. Besides, when the preheating temperatures are below 120 °C, $\widetilde{\mu}_i$ is nearly zero, indicating that a low storage temperature below 120 °C can effectively reduce material degradation.

Fig. 17 shows comparisons of $\widetilde{\mu}_i$ at 1200 s between (a) Samples with different preheating temperatures, and (b) Preheating temperatures for different samples. At 90 °C, $\widetilde{\mu}_i$@1200 s approaches to zero, leading to almost no degradation for the material at this temperature (Fig. 17b). $\widetilde{\mu}_i$@1200 s decreased evenly with decreasing preheating temperatures (Fig. 17a). At high temperatures (150 °C–160 °C), the differences of $\widetilde{\mu}_i$@1200 s between different samples are large; those differences reduce quickly at lower temperatures below 120 °C (Fig. 17b).

4. Conclusions

In SLS, a considerable amount of expensive polyamide 12 powders remains un-sintered but reusable after going through severely irreversible chemical degradations. The degradation originates from the thermal energy controlled by the coupled oxygen and laser effects. Through experimentation, and by fitting the actual SLS degradation rates to the basic autoxidation model, we obtained the coefficients of coupled oxygen and laser effects. A further sensitivity analysis suggests the existence of a polynomial fitting between the sample degradation rates and oxidation time. From there, we propose a new kinetic scheme for SLS degradation of polyamide 12 composed of the basic autoxidation model, the coefficients of coupled oxygen and laser effects, and the relationships between the sample degradation rates and oxidation time. The new model can predict the oxidation rates of pure or mixed (different degradation levels) polyamide 12 using two easily available parameters: materials density and oxidation time. The predicted degradations from the proposed kinetic model match on average 89.53% with the actual SLS degradation rates, in contrast to a 34.48% accuracy from a conventional aging model. We found that the laser effects are 4-time stronger than oxygen effects on polyamide 12 degradation. Furthermore, we identified the influences of the coupled oxygen and laser effects in SLS and preheating temperatures on the degradation rates. The findings provide a first-instance knowledge of quantitative material degradation related to the estimated parameters, and insights to reduce degradation in SLS. This work established a novel effective model to obtain the kinetic scheme of polyamide 12 degradation to aid future studies of materials degradation and reuse in the SLS process.

Declaration of competing interest

The authors declare that they have no known competing financial interests or personal relationships that could have appeared to influence the work reported in this paper.

Acknowledgments

This work was supported in part by National Science Foundation Award 1953155.

References

[1] Balemans C, Looijmans SF, Grosso G, Hulsen MA, Anderson PD. Numerical analysis of the crystallization kinetics in SLS. Addit Manuf 2020;33:101126.
[2] Sindinger S, Kralovec C, Tasch D, Schagerl M. Thickness dependent anisotropy of mechanical properties and inhomogeneous porosity characteristics in laser-sintered polyamide 12 specimens. Addit Manuf 2020;33:101141.
[3] Ngo TD, Kashani A, Imbalzano G, Nguyen KT, Hui D. Additive manufacturing (3D printing): a review of materials, methods, applications and challenges. Compos Part B Eng 2018;143:172–96.
[4] Wudy K, Drummer D. Aging effects of polyamide 12 in selective laser sintering: molecular weight distribution and thermal properties. Addit Manuf 2019;25:1–9.
[5] Bakshi KR, Mulay AV. A review on selective laser sintering: a rapid prototyping technology. IOSR J Mech Civ Eng 2016;4:53–7.
[6] Kruth J, Wang X, Laoui T, Froyen L. Lasers and materials in selective laser sintering. Assem Autom 2003;23(4):357–71.
[7] Paolucci F, Mook M van, Govaert LE, Peters G. Influence of post-condensation on the crystallization kinetics of PA12: from virgin to reused powder. Polymer 2019;175:161–70.
[8] Majewski C, Zarringhalam H, Hopkinson N. Effect of the degree of particle melt on mechanical properties in selective laser-sintered Nylon-12 parts. Proc Inst Mech Eng B J Eng Manuf 2008;222(9):1055–64.
[9] Drummer D, Wudy K, Kühnlein F, Drexler M. Polymer blends for selective laser sintering: material and process requirements. Phys Procedia 2012;39:509–17.
[10] Drummer D, Rietzel D, Kühnlein F. Development of a characterization approach for the sintering behavior of new thermoplastics for selective laser sintering. Phys Procedia 2010;5:533–42.
[11] Schmid M, Amado A, Wegener K. Polymer powders for selective laser sintering (SLS). AIP Conf Proc 2015;1664.
[12] Chen P, Tang M, Zhu W, Yang L, Wen S, Yan C, et al. Systematical mechanism of polyamide-12 aging and its micro-structural evolution during laser sintering. Polym Test 2018;67:370–9.
[13] Dadbakhsh S, Verbelen L, Verkinderen O, Strobbe D, Puyvelde P Van, Kruth J. Effect of PA12 powder reuse on coalescence behaviour and microstructure of SLS parts. Eur Polym J 2017;92:250–62.
[14] Dotchev K, Yusoff W. Recycling of polyamide 12 based powders in the laser sintering process. Rapid Prototyp J 2009;15(3):192–203.
[15] El-Mazry C, Hassine MB, Correc O, Colin X. Thermal oxidation kinetics of additive free polyamide 6-6. Polym Degrad Stab 2013;98(1):22–36.
[16] Drummer D, Wudy K, Drexler M. Modelling of the aging behavior of polyamide 12 powder during laser melting process. AIP Conf Proc 2015;1664.
[17] Gornet TJ, Davis KR, Starr TL, Mulloy KM. Characterization of selective laser sintering materials to determine process stability. Int Solid Freeform Fabr Symp 2002:546–53.
[18] Zarringhalam H, Hopkinson N, Kamperman NF, Vlieger JJ De. Effects of processing on microstructure and properties of SLS nylon 12. Mater Sci Eng A 2006;435:172–80.
[19] Wang L, Kiziltas A, Mielewski DF, Lee EC, Gardner DJ. Closed-loop recycling of polyamide12 powder from selective laser sintering into sustainable composites. J Clean Prod 2018;195:765–72.
[20] Feng L, Wang Y, Wei Q. PA12 powder recycled from SLS for FDM. Polymers 2019;11(4):727.
[21] Diller TT, Yuan M, Bourell DL, Beaman JJ. Thermal model and measurements of polymer laser sintering. Rapid Prototyp J 2015;21(1):2–13.
[22] Yuan M, Diller TT, Bourell D, Beaman J. Thermal conductivity of polyamide 12 powder for use in laser sintering. Rapid Prototyp J 2013;19(6):437–45.
[23] Bernard S, Youinou L, Gillard P. MIE determination and thermal degradation study of PA12 polymer powder used for laser sintering. J Loss Prev Process Ind 2013;26(6):1493–500.
[24] Gillen KT, Wise J, Clough RL. General solution for the basic autoxidation scheme. Polym Degrad Stab 1995;47(1):149–61.
[25] Rincon-Rubio LM, Fayolle B, Audouin L, Verdu J. A general solution of the closed-loop kinetic scheme for the thermal oxidation of polypropylene. Polym Degrad Stab 2001;74(1):177–88.
[26] Colin X, Fayolle B, Audouin L, Verdu J. About a quasi-universal character of unstabilised polyethylene thermal oxidation kinetics. Polym Degrad Stab 2003;80(1):67–74.
[27] Colin X, Audouin L, Verdu J. Determination of thermal oxidation rate constants by an inverse method. Application to polyethylene. Polym Degrad Stab 2004;86(2):309–21.
[28] Laun S, Pasch H, Longiéras N, Degoulet C. Molar mass analysis of polyamides-11 and-12 by size exclusion chromatography in HFiP. Polymer 2008;49(21):4502–9.
[29] Khelidj N, Colin X, Audouin L, Verdu J, Monchy-Leroy C, Prunier V. Oxidation of polyethylene under irradiation at low temperature and low dose rate. Part II. Low temperature thermal oxidation. Polym Degrad Stab 2006;91(7):1598–605.